Performance of Mixture-Ratio-Controlled Hybrid Rockets for Nominal Fuel Regression

Kohei Ozawa[1] and Toru Shimada[2]
Institute of Space and Astronautical Science, JAXA, Sagamihara, Kanagawa, Japan, 252-5210

This article discusses the impacts of O/F shifts on flight performance of single-stage sounding rockets using flight simulations of three scales of O/F-controlled and -uncontrolled hybrid rockets under a nominal fuel regression behavior without uncertainty. The flight simulation code includes three factors dependent on O/F ratio: thermodynamic states of the burnt gas (theoretical I_{sp}), shifts in c^* efficiency, and nozzle throat erosion. In the flight simulations, a thrust control law was applied to increase the apogee and evaluate effects of O/F shifts in the thrust curve including throttling. For the best cases in each scale, O/F-controlled hybrid rockets slightly improved the performance by 2.03-2.42% in averaged specific impulse. However, the performance of the O/F-controlled sounding rockets is essentially the same as the O/F-uncontrolled type under the median regression behavior, especially when considering the slight increases in the mass and complexity of the oxidizer feed system needed for O/F control. Considerable scale effects on throat erosion and theoretical I_{sp} were observed, but that of c^* efficiency was negligible. The improvement of theoretical I_{sp} was the primary contributor to flight performance, responsible for a larger than 70% share in the total I_{sp} increase. The second largest contribution was the improvement of c^* efficiency with a share of 21.8-24.3%. The O/F control gave the improvement of throat erosion corresponding to 5.75% in the total I_{sp} increase for the smallest scale, but with increasing the scale, the throat area increase ratio became small so that the throat erosion improvement contribution was reduced to 1.21%.

[1] Assistant Professor, Department of Mechanical and Control Engineering, Faculty of Engineering, Kyushu Institute of Technology, 1-1, Senshi-cho, Tobata-ku, Kitakyushu City, Fukuoka, Japan, 804-8550, AIAA Member.
[2] Professor, Department of Space Flight Systems, Institute of Space and Astronautics, Japan Aerospace Exploration Agency, 3-1-1, Yoshinodai, Chuo-ku, Sagamihara City, Kanagawa, AIAA Associate Fellow.

Nomenclature

A	=	cross-sectional area [m^2]
a_0	=	regression rate coefficient for axial hybrid rockets or sound velocity at sea level [m/s]
A_i	=	frequency factor of Arrhenius equation
AR	=	total aspect ratio including oxidizer tank and solid fuel [-]
b_i	=	temperature exponent [-]
c	=	molecular density [mol/m^3]
c^*	=	characteristic velocity [m/s]
C_D	=	aerodynamic drag coefficient [-]
D	=	aerodynamic drag [N]
$D_{i,air}$	=	diffusion coefficient of i-th species in air [m^2/s]
D_t	=	nozzle throat diameter [m]
E	=	activation energy [J/mol]
f	=	switching function for thrust control [-]
F	=	thrust [N]
$(F/W)_i$	=	initial thrust-to-weight ratio [-]
g	=	gravitational acceleration at sea level [m/s^2]
G	=	mass flux [kg/m^{2}s]
G_{e_i}	=	mass flux erosion spent for i-th oxidizing chemical species [kg/m^{2}s]
h	=	enthalpy per unit mass [J/kg]
I_{sp}	=	specific impulse [s]
$\overline{I_{sp}}$	=	time-averaged specific impulse [s]
k	=	inverse of time constant [s^{-1}]
$\bar{k}$	=	non-dimensional time constant [-]
k_i	=	coefficient in erosion rate equation Eq. (19)
L	=	length [m]
L^*	=	characteristic length [m]
L_o	=	length of oxidizer tank [kg]

m	=	mass [kg]
M	=	molecular weight [kg/mol] or Mach number at the sea level [-]
$\dot{m}$	=	mass flow rate [kg/s]
m_{sf}	=	initial fuel mass [kg]
m_o	=	initial oxidizer mass [kg]
N	=	molecular flux [mol/m²s]
n_1, n_2	=	regression rate exponents corresponding to oxidizer mass flux and geometric swirl number [-]
n_i	=	reaction rate exponent for i-th oxidizing chemical species [Pa]
O/F	=	oxidizer-to-fuel mass ratio [-]
p	=	pressure [Pa]
p_i	=	partial pressure of i-th oxidizing chemical species [Pa]
r	=	radius [mm]
R	=	gas constant [J/kgK]
$\dot{r}$	=	regression rate [m/s]
$\dot{r}_t$	=	throat erosion rate [m/s]
R_e	=	Reynolds number [-]
R_μ	=	universal gas constant [J/molK]
s	=	entropy per unit mass [J/kgK]
S_c	=	Schmidt number [-]
S_g	=	geometric swirl number [-]
t	=	time [s]
T	=	temperature [K]
u	=	gaseous velocity [m/s]
v	=	velocity of rocket [m/s]
V	=	volume [m³]
x	=	molecular fraction [-] or altitude of rocket [m]
$\boldsymbol{x}$	=	state vector
z	=	distance from nozzle throat wall [m]

α	=	sensitivity of c^* efficiency to S_g [-]
γ	=	heat capacity ratio [-]
δ	=	concentration boundary layer thickness [m] or threshold of thrust control [-]
η_{c^*}	=	c^* efficiency [-]
$\eta_{c^*{}_\infty}$	=	c^* efficiency of an axially-injected hybrid rocket when $\bar{L}^* \to \infty$ [-]
λ	=	adjoint vector
ρ	=	density [kg/m^3]
ρ_o	=	density of liquid oxidizer [kg/m^3]
τ_i	=	time scale [s]
τ_{stay}	=	staying time of propellant inside combustion chamber [s]
φ	=	radius ratio based on throat radius [-]

Subscripts

0	=	core flow, sea level, or lift-off
a	=	ambient
ave	=	averaged
c	=	combustion chamber
c*	=	c^* efficiency
e	=	at nozzle exit or with throat erosion
fin	=	final
i	=	ideal, initial, or i-th chemical species
in	=	inner side of a cylinder
inj	=	injector
j	=	j-th chemical species
k	=	a chemical species
m	=	moment arm
max	=	maximum
mid	=	after the state vector has reached the singular surface

min	=	minimum
n	=	nozzle
o	=	oxidizer
out	=	outer side of a cylinder
p	=	fuel port
pc	=	pre-combustion chamber
ref	=	referential
s	=	singular surface
sep	=	threshold to prevent flow separation at the nozzle exit
sf	=	solid fuel
t	=	nozzle throat
w	=	nozzle throat wall

I.   Introduction

Conventional hybrid rocket propulsion always has a possibility to cause a shift in oxidizer to fuel ratio (O/F) during engine operation if there are no countermeasures to maintain the O/F ratio. This phenomenon is called "O/F shift". We could not find any previous studies on hybrid rocket propulsion which comprehensively classified both types of O/F shifts and factors dependent on O/F and affecting propulsive performance in detail. In most studies which mention O/F shifts [1][2][3], it was assumed that port expansion and throttling only cause O/F shifts under an ideal fuel regression behavior without any errors, and O/F shifts decrease the performance only due to the shift in the enthalpy per unit mass of the product gas, which affects ideal c^* and exit velocity. These previous investigations did not cover all the sources or effects of O/F shifts. They conclude that O/F shifts are negligible or shifts in enthalpy can cause a considerable performance loss only for deep throttling [3]. Barato et al. [4] challenged such an established theory by proposing and evaluating the performance decrease due to the residual propellant caused by the uncertainty of the median fuel regression behavior or the errors of the actual oxidizer mass flow rate history from the planned one. However, they also assumed that O/F shifts decrease the propulsive performance only via the shift in the enthalpy of the product gas.

We believe that the previous discussion lacks consideration of the sources and effects of O/F shifts under the ideal fuel regression behavior and rocket performance calculation. For example, an error in solid fuel regression from a nominal regression curve yields an instantaneous O/F shift. An O/F shift causes a shift of ideal L^* to reach the chemical equilibrium of burnt gas, leading to a shift of c^* efficiency. The O/F shift also causes a shift in mole fractions of the product gas, resulting in a shift in throat erosion rates. These factors should also affect the rocket performance.

This paper has two purposes: 1) modeling the factors affected by O/F shifts along with the median (nominal) regression curve and integrating these models into a flight simulation of hybrid sounding rockets; 2) evaluating the effects of O/F shifts on the comprehensive performance of hybrid rocket propulsion.

Our study starts with modeling the nominal fuel regression curve and the physical phenomena affected by O/F shifts (the shift in the enthalpy per unit mass of the product gas, c* efficiency, and nozzle throat erosion). The latter models are validated with experimental results and implemented into a flight simulation code, which evaluates the effects of O/F shifts on the flight performance of hybrid sounding rockets including throttling. Here we should note that this paper assumes a nominal fuel regression behavior so that this study only considers the O/F shifts on a nominal fuel regression curve without errors. However, the methodology developed in this study will also be applicable to the cases where anomalies or uncertainties in the fuel regression cause a propellant residual mass, resulting in a decrease in the total ΔV.

The effects of O/F shifts on flight performance are evaluated by comparing the performance between O/F-controlled and –uncontrolled hybrid rockets. This study applied Altering-intensity Swirling Oxidizer Flow Type (A-SOFT) [5] for the O/F control method because A-SOFT motors exhibit greater combustion stability and higher baseline regression rates than the alternatives. This type used the sensitivity of regression rates on geometric swirl number for the O/F control. A-SOFTs have axial and tangential injectors, of which oxidizer mass flow rates are independently controlled as shown in Fig. 1. The O/F control independent of thrust is possible by the "dual injector" controlling the effective swirl number. On the other hand, sounding rockets with Swirling Oxidizer Flow Type (SOFT) [6] hybrid rocket engines are also simulated as the conventional O/F-uncontrolled rockets for comparison. This type has the same level of regression rates, but O/F is not controlled because this type only has a tangential injector.

This study focuses only on the case studies of a single-stage sounding rocket mission in various applications of rocket propulsion. This is because a sounding rocket mission is a major application to demonstrate new concepts of large-scale rocket engines on the way of development of satellite-launchers, and this mission requires throttling to

achieve an altitude as high as possible with a finite propellant mass when considering gravitational acceleration and aerodynamic drag. The dimensions of the rockets are determined by the relations among thrust-to-weight ratio at the lift-off, dimensions of the solid fuel grains and oxidizer tank, and density of the propellants. The one-dimensional vertical ascent is simulated to simplify the simulations, and a few performance variables such as the apogee and specific impulse are compared between O/F-controlled and –uncontrolled types. These analyses reveal which O/F-dependent phenomena have large impacts on flight performance and whether the performance loss due to O/F shifts is crucial to the overall total performance under the nominal fuel regression.

II.   Modeling of Fuel Regression Behavior

In this section, fuel regression rate behavior is analyzed from previous experimental data, and we model the fuel regression rate behavior for SOFTs and A-SOFTs. In our flight simulations, paraffin wax and gaseous oxygen (GOX; stored as liquid phase) are selected as the propellants because of high baselines of regression rates. However, there is little previous data with paraffin wax and GOX available to model the dependence on swirl number. The two accessible papers by Nakagawa et al. [7] and Saito et al. [8] reported that paraffin-based fuels have higher sensitivity to geometric swirl number than other conventional fuels especially in the front region of the grain. In spite of these valuable results, due to small numbers of experimental conditions and data, it remains too difficult to reliably model fuel regression behavior with only this data. Therefore, in this section, we model a "virtual" fuel regression behavior combining the two datasets of axial hybrid rocket motors with paraffin and GOX and SOFTs with polymethyl methacrylate (PMMA) and GOX.

The dataset of axial hybrids with paraffin and GOX were quoted from the paper by Karabeyoglu et al. [9]. This paper shows 69 data points over the broad range of averaged oxidizer mass flux from 15 to 370 [kg/m^{2}s]. For SOFTs, the two datasets with PMMA and GOX by Yuasa's group [6] have a relatively wide range of geometric swirl number from 0 to 32.3. Geometric swirl number is defined as the following equations as

$$S_g = \frac{r_m \rho_{inj} u_{inj}^2 A_{inj}}{r_{pc} \rho_{inj} u_{pc}^2 A_{pc}} = \frac{r_m A_{pc}}{r_{pc} A_{inj}} \tag{1}$$

where R_m refers to moment arm of the injector ports, the subscripts "inj" and "pc" refer to injector port and pre-chamber, respectively. r_{pc} refers to the axial velocity of oxidizer in the pre-combustion chamber. The above equation was transformed under the assumptions of incompressible flow and the mass conservation law of $\rho_{inj} u_{inj} A_{inj} = \rho_{inj} u_{pc} A_{pc}$. These experiments measured the regression rates averaged over the burn time and the port length. We

used the regression rate equation proposed by Tamura et al. [10] extended for the sensitivity to geometric swirl number as

$$\dot{r}(t) = a_0 G_o(t)^{n_1}\left(\left\{1 + S_g(t)^2\right\}\right)^{n_2} \tag{2}$$

where $\dot{r}(t)$, a_0, n_1, and n_2 refer to instantaneous regression rate, regression rate coefficient for $S_g = 0$, and constant exponents characterizing the sensitivity to instantaneous oxidizer mass flux $G_o(t)$ and geometric swirl number $S_g(t)$, respectively. It is also possible to approximate the regression rate behavior of A-SOFTs with this model, and we apply this equation for paraffin and GOX here. In our simulation, a_0 and n_1 for paraffin and GOX and n_2 for PMMA and GOX were used for a "virtual" regression rate behavior assuming SOFTs and A-SOFTs with paraffin wax and GOX. The median values of (a_0, n_1, n_2) were analyzed with the multiple linear regression [11] of these experimental data. The results of (a_0, n_1, n_2) for $\dot{r}$ in mm/s and G_o in kg/m^{2}s were (exp(-2.22), 0.640, -) for axial injection with paraffin and GOX and (exp(-3.70), 0.616, 0.156) for swirling injection of PMMA and GOX, respectively (n_2 is not defined for axial injection). Therefore, the nominal fuel regression rate model:

$$\dot{r} = \exp(-2.22)\, G_o^{0.640}\left(1 + S_g^2\right)^{0.156} \tag{3}$$

was used for the A-SOFT and SOFT with paraffin and GOX in this paper.

III.   Modeling of Performance Factors in Hybrid Rocket Engines Affected by O/F Shifts

As discussed in the first section, O/F shifts along with the nominal regression curve have a possibility to affect three factors in a propulsive subsystem. We model these three factors based on theoretical consideration and experimental results. Especially for c^* efficiency and nozzle throat erosion, models possible to implement into a flight simulation code are validated with existing experimental results.

A. Chemical Equilibrium and Nozzle Flow Models

Our flight simulation program conceptually calculates the chemical equilibrium state of the product gas of the injected oxidizer and the regressed fuel to evaluate the propulsive performance of its ideal nozzle flow. This chemical equilibrium state is calculated using our in-house code of Gibbs Energy minimization under the assumption of a perfect gas except for condensed chemical species such as graphite. This code was developed using the technical report by Gordon and McBride [12] and validated with NASA CEA [13]. The thermodynamic data table of 1-octene C_8H_{16} was substituted for that of paraffin wax fuel in our analyses. The product gas was assumed to consist of the 11 species:

CH_4, O_2, H_2O, CO_2, H_2, CO, OH, O, H, C_2H_2, and C (solid graphite). The former 9 species are often assumed to exist in CFDs assuming local chemical equilibrium of the burnt gas of hydrocarbon and oxygen, but non-negligible mole fractions of the latter two species are included in the results of NASA CEA at high equivalence ratios larger than 5. These two species provide robustness of chemical equilibrium calculation when simulating the cases with errors in the fuel regression model. All the thermodynamic data in our program is calculated by the polynomial approximations of molar standard-state thermodynamic data [14].

The initial conditions are given at the beginning of the in-house code. They are thermodynamic properties and state of the fuel and oxidizer, oxidizer mass flow rate, geometric swirl number, fuel regression rate equation, dimensions of the solid fuel grain and nozzle, and a target chamber pressure temporarily given. Dynamic pressure of the oxidizer flow is ignored here. The chemical equilibrium at the given chamber pressure is sought by the iteration of the Gibbs Energy minimization, and the result is checked by the following choking condition equation at the nozzle:

$$G_t = \frac{p_c}{\sqrt{R_c T_c}} \sqrt{\gamma \left(\frac{2}{\gamma+1}\right)^{\frac{\gamma+1}{\gamma-1}}} \tag{4}$$

where G_t, γ, R, and T_c refer to mass flux of the propellant at the nozzle throat, specific heat ratio, gas constant, and temperature of the burnt gas at the combustion chamber, respectively. G_t is calculated from the mass flow rate of the fuel and the nozzle throat, and the other properties are calculated from the result of the chemical equilibrium state. The equilibrium calculation is iterated with a different chamber pressure until Eq. (4) is satisfied. Equation (4) suggests that this model assumes a frozen flow at least from the combustion chamber to the nozzle throat. Our flight simulation also assumed a frozen flow downstream of the throat. Nozzle exit pressure p_e and thrust F are calculated from the following ideal isentropic flow as

$$\begin{cases} \dot{m}_c = A_e \rho_e u_e \\ h_c(T_c) = \frac{1}{2} u_e^2 + h_e(T_e) \\ s_c(p_c, T_c) = s_e(p_e, T_e) \end{cases} \tag{5}$$

and

$$F = \dot{m} u_e + (p_e - p_a) A_e \tag{6}$$

where A, F, $\dot{m}$, p, h, s, and u refer to area, thrust, mass flow rate of propellant, pressure, specific enthalpy, entropy, and velocity, respectively, and the subscripts a, c, and e refer to ambient, combustion chamber, and nozzle exit, respectively.

B. c^* Efficiency Model

After calculating the ideal performance, c^* efficiency is evaluated with a simple method by modifying that for liquid rocket propulsion. For liquid propulsion, c^* efficiency is typically evaluated by a characteristic chamber length L^* [15] to relate mixing and chemical reaction rates with the design of the combustion chamber. The propellants injected into the combustion chamber need a residence time τ_i to achieve a sufficient c* efficiency near to chemical equilibrium there. This reference residence timescale τ_i can be approximated by the corresponding reference chamber volume V_{c_i} , a density of the product gas ρ_c, propellant mass flow rate $\dot{m}$, nozzle throat area A_t and mass flux at nozzle throat G_t:

$$\tau_i \sim \frac{V_{c_i}}{\dot{m}/\rho_c} = \left(\frac{V_c}{A_t}\right)_i \frac{\rho_c}{G_t} = L_i^* \frac{\rho_c}{G_t} \tag{7}$$

where $L^* = V_c/A_t$. When the thermodynamic state of the chamber gaseous flow is represented by that at chemical equilibrium, the perfect gas state equation, Eq. (4), and Eq. (7) provide the reference characteristic length L_i^* based on V_{c_i} as

$$L_i^* \sim \tau_i \sqrt{\gamma R_c T_c \left(\frac{2}{\gamma+1}\right)^{\frac{\gamma+1}{\gamma-1}}} \tag{8}.$$

Originally, the timescale τ_i should include both the diffusion and kinetic timescale in liquid propulsion, but the latter should be dominant for engines with well-designed injectors. Therefore, τ_i is approximately determined by the fuel and oxidizer so that the scale of L_i^* can be approximately estimated by τ_i related to the time constant of the chemical reaction and the equilibrium thermodynamic state of the product gas, that is dependent on O/F ratio. Assuming that the gaseous velocity in the combustion chamber with L_i^* is the same as that in the chamber with L^*, actual-to-ideal residence time ratio is roughly expressed by

$$\tau_{stay}/\tau_i \sim L^*/L_i^* \equiv \bar{L}^* \tag{9}$$

where τ_{stay} refers to actual residence time. Here, we assumed that c^* efficiency is equivalent to the completeness to the reaction without considering heat loss. If the combustion is characterized by a first-order reaction, c^* efficiency η_{c^*} is roughly estimated by

$$\eta_{c^*} = \frac{c^*}{c_i^*} = 1 - \exp(-k\tau_{stay}) = 1 - \exp\left\{-(k\tau_i)\frac{\tau_{stay}}{\tau_i}\right\} \approx 1 - \exp(-\bar{k}\bar{L}^*) \tag{10}$$

where k and $\bar{k}$ refer to reaction rate constant and that normalized by τ_i, respectively. This c^* efficiency model was validated with an experimental result of a liquid rocket engine with Aerozine-50 and N_2O_4 [15]. Fig. 2 a) shows that

Eq. (10) for $\bar{k} = 6.6$ approximated the test results well. Here we should note that the two largest experimental results had a larger c* than the theoretical value calculated by NASA CEA [12], 1736.9 [m/s]. Therefore, the largest c* in Ref. [15] and the corresponding L^* were assumed to be the c* with the 100% c* efficiency and L^*_i, respectively.

Conversely, for hybrid rocket propulsion, it is said that the boundary layer combustion in hybrid rockets is rather dominated by the diffusion timescale in the turbulent boundary layer [16], which is an order of magnitude higher than the kinetic timescale [16]:

$$\tau_i \sim \begin{cases} 10^{-2} - 10^{-1}[s] & \text{(Diffusion timescale)} \\ 10^{-3} - 10^{-2}[s] & \text{(Gaseous kinetic timescale)} \end{cases} \tag{11}.$$

Equation (11) says that L^*_i of hybrid rocket engines can be up to 100 times larger than that of well-designed liquid rocket engines. Moreover, there can be a substantial upper limit of c* efficiency in axially-injected wax-based hybrid rockets. Figure 2 b) shows the two datasets of c* efficiency of the axially-injected wax-based hybrid rockets by Nakagawa et al. [17] and Karabeyoglu et al. [9]. Here it should be noted that $\bar{L}^*$ was evaluated with the L^*_i of 10 times longer length than that for liquid rocket engines with liquid oxygen and RP-1 [15] because Ref. [17] did not show detailed results like each O/F ratio and regression rate. L^* was evaluated with $L^* = (\pi r_p^2 L_{sf} + 2V_{pc})/(2A_t)$ assuming that the fuel is injected at the center of the fuel port. These two datasets seemed to draw a smooth curve, however, c* efficiency reached just 0.88 even when the $\bar{L}^*$ is 0.7 to 0.8. In this paper, in order to express the substantial upper limit, Eq. (10) was modified as

$$\eta_{c^*} = \eta_{c^*\infty}\{1 - \exp(-\bar{k}\bar{L}^*)\} \tag{12}$$

where $\eta_{c^*\infty}$ is the substantial upper limit of c* efficiency. This approximation fits the experimental data better than Eq. (12), and the resultant values of $\eta_{c^*\infty}$ and $\bar{k}$ were 8.25×10^{-1} and 20.3, respectively. Our model is intended to simply apply the c^* efficiency of liquid propulsion for that of hybrid rocket propulsion with the diffusion timescale, but this estimation succeeded in the rough estimation. Considering the difference in τ_i used in the analyses, the $\bar{k}$ of 20.3 is 3.25 times larger than for liquid rocket propulsion, which is within the difference of the order of magnitude between the two time scales.

c^* efficiency depends also on geometric swirl number [5] because the circumferential velocity component enhances the mass transfer in the boundary layer, and the centrifugal force driven by the swirling flow transports the unburned propellants with large densities toward the wall of the port. c^* efficiency of lab-scale SOFTs with paraffin and gaseous oxygen [18] is also plotted in Fig. 2 when $S_g = 19.4$. The SOFTs had high c* efficiencies; more than 90% even when

$\bar{L}^* < 0.2$. In this study, Eq. (12) was further modified to empirically approximate this effect by assuming $\eta_{c^*{}_\infty}$ is a linear function of S_g. The linear sensitivity to S_g was chosen because of the lack of experimental data for various S_g. The modified function is

$$\eta_{c^*} = \min\left((\alpha S_g + \eta_{c^*{}_\infty})\{1 - \exp(-\bar{k}\bar{L}^*)\},\ 1\right) \tag{13}$$

where α is 8.03×10^{-3} as a result of curve fitting. This curve fitting agreed well with both experimental data of the axial and swirling hybrids as shown in Fig. 2 b), and η_{c^*} converges to 9.81×10^{-1} when $\bar{L}^* \to \infty$ and $S_g = 19.4$.

In the flight simulation code, L^* in Eq. (13) is replaced by using fuel port diameter r_p because the fuel is injected over the solid fuel port. Here L^*_{pc} refers to the characteristic length of the post-chamber. Finally, the c* efficiency model used in the flight simulation code is summarized in the following set of equations:

$$\begin{cases} \eta_{c^*} = \min\left((\alpha S_g + \eta_{c^*{}_\infty})\{1 - \exp(-\bar{k}\bar{L}^*)\},\ 1\right) \\ \bar{L}^* = \frac{\pi r_p^2 L_{sf} + 2V_{pc}}{2A_t L_i^*} \\ c_i^* = \frac{p_{c_i}}{A_t \dot{m}} \\ L_i^* = 10^{-2}\sqrt{\gamma R T_c \left(\frac{2}{\gamma+1}\right)^{\frac{\gamma+1}{\gamma-1}}} \end{cases} \tag{14}.$$

C. Nozzle Throat Erosion Model

Here we develop a chemical erosion model of the nozzle throat simple enough to use in flight simulation codes of hybrid rockets. Hybrid rocket propulsion tends to have larger erosion rates of the graphite nozzle throat than solid propulsion because mole fractions of chemical species which oxidize graphite are larger than those for solid propulsion. Chemical erosion was only considered here because condensed phase species should scarcely be included in the resultant product after the chemical reaction assuming a high c^* efficiency. The dependency of the throat erosion rate on swirl number was ignored in this paper because 1) the high baseline of regression rates of wax-based fuels was expected to require small geometric swirl numbers in the flight simulation, compared to the test conditions of the only available data we found [19]; 2) the erosion rates of Ref. [19] measured only the time-averaged values and did not measure the throat surface temperature, which is an important factor to determine erosion rates.

Throat erosion rates mainly depend on chamber pressure (or mass flux at the throat) and O/F ratio because throat erosion rate is considered to be determined by the balance between the supply of oxidizing species to the concentration

boundary layer due to molecular diffusion and the chemical reaction of the solid graphite with the oxidizing species at the wall as shown in Fig. 3. In the field of solid rocket propulsion with hydrocarbon fuels, chemical erosion of nozzle throat at thermal equilibrium state in combustion flows is dominated by the following 5 chemical reactions [20] as

$$\begin{cases} C(s) + CO_2 \rightarrow 2CO \\ C(s) + \frac{1}{2}O_2 \rightarrow CO \\ C(s) + H_2O \rightarrow CO + H_2 \\ C(s) + OH \rightarrow CO + H \\ C(s) + O \rightarrow CO \end{cases} \tag{15}.$$

In this paper, the molecular diffusion model by Delaney et al. [21] was adopted to evaluate the molecular flux of the oxidizing species to the throat wall. This model is a simplified one-dimensional Fick's law [22] to calculate the molecular flux in the concentration boundary layer:

$$N_i = -cD_{i,air}\frac{dx_i}{dz} + x_i(N_i + N_j) \tag{16}$$

where c, N, and x refer to molecular density, molecular flux, and molecular fraction, and the subscripts i and j refer to oxidizing species and product species, respectively. $D_{i,air}$ refers to the binary diffusion coefficient between an oxidizing species i and the burnt gas, but it was substituted by the diffusion coefficient in the air in their study. In addition to this rough approximation, the second term on the right hand side was approximated into the above form though it should be the total molecular flux of all the species for the simplicity of calculations. We also followed these approximations for the fast calculation. The diffusion coefficients were estimated using the references [23] and [24]. When the diffusion coefficients were estimated, the temperature of the core flow at the throat was replaced by a 5% higher value than the actual calculation to account for temperature recovery in the compressible boundary layer. The exact solution of Eq. (16) is

$$N_i = \begin{cases} \frac{cD_{i,air}}{\delta}\ln\left(\frac{1+x_{i0}}{1+x_{iw}}\right) & (O_2, CO_2, H_2O, OH) \\ \frac{cD_{i,air}}{\delta}(x_{i0} - x_{iw}) & (O) \end{cases} \tag{17}$$

where δ refers to concentration boundary layer thickness, and the subscripts 0 and w refer to boundary conditions at the outer edge of the concentration boundary layer and the wall, respectively. The boundary condition at the outer edge was given by the result of the Gibbs Energy minimization under the sonic condition. Delaney et al. [21] evaluated δ using the Gilliland-Sherwood equation [25] as

$$\frac{D_t}{\delta} = 0.023R_e^{0.81}S_c^{0.44} \tag{18}$$

where Reynolds number R_e and Schmidt number S_c are defined as DG_t/μ and $\mu/(D_{i,air}\bar{M})$, and $\bar{M}$ refers to the averaged molecular weight of the core flow.

The oxidizing species fed by the molecular diffusion react at the wall of the nozzle throat with their finite reaction rates. Here, the chemical reaction rate by Chelliah et al. [20] was adopted for the chemical reaction model. This model gives the mass flux of i-th oxidizing species reacting at the throat surface:

$$\begin{cases} G_{e1}=\frac{k_1 p_1 Y}{1+k_2 Y}+k_3 p_1(1-Y) \\ Y=\left(1+\frac{k_4}{k_3 p_1}\right)^{-1} \\ G_{ei}=k_j p_i^{n_i} \ (i=2\sim5, j=i+3) \end{cases} \tag{19}$$

where G_{e_i} and p_i refer to i-th reacting mass flux and partial pressure, respectively. k_j refers to a rate constant for each reaction modeled by the Arrhenius equation as

$$k_j = A_j T_w^{b_j} \exp\left(-\frac{E_j}{R_\mu T_w}\right) \tag{20}$$

where A_j, b_j, and E_j are constants for each reaction. These parameters are listed in reference [20].

The balance between Eq. (17) and Eq. (19) with the stoichiometric ratios of the reactions Eq. (15) provides the following equations to solve the unknown variables x_{iw} at the quasi-steady state:

$$\begin{cases} \frac{k_1 p_t x_{O_2 w} Y}{1+k_2 Y} + k_3 p_t x_{O_2 w}(1-Y) = 2M_c \frac{c D_{O_2,air}}{\delta}\ln\left(\frac{1+x_{O_2 0}}{1+x_{O_2 w}}\right) \\ k_j(p_t x_{iw})^{n_i} = M_c \frac{c D_{i,air}}{\delta}\ln\left(\frac{1+x_{i0}}{1+x_{iw}}\right) \quad (CO_2, H_2O, OH) \\ k_j(p_t x_{Ow})^{n_O} = M_c \frac{c D_{O,air}}{\delta}(x_{O0} - x_{Ow}) \end{cases} \tag{21}$$

where M_c refers to the molecular weight of the graphite nozzle throat. The resultant throat erosion rate $\dot{r}_t$ is calculated from G_{e_i} yielded by Eq. (17):

$$\dot{r}_t = \sum_{i=1}^{5}\frac{G_{e_i}}{\rho_n} \tag{22}$$

where ρ_n refers to the density of the graphite nozzle throat and was $1.7 \times 10^3 [kg/m^3]$ in our code.

Our erosion model was validated with the experimental results of Kamps et al. [26]. They estimated throat erosion rates for various O/Fs using their test results of hybrid rocket motors. The concept of their technique is to estimate the performance histories unable to be acquired directly by measurement systems over a burn by using a linear regression of a test using directly measured data and NASA CEA [13] under the assumption of a constant c^* efficiency. Their research is characterized also by estimating instantaneous erosion rates for various instantaneous equivalence ratios from a single test positively utilizing O/F shifts of hybrid rocket motors. Our model was validated with the two test

results during which the instantaneous equivalence ratio crossed the stoichiometric ratio. Our calculation was carried out with the averaged throat diameter and the averaged chamber pressure listed in their paper.

Figures 4 a) and b) show the comparisons of erosion rates between our erosion model and the experimental results. These figures show the calculation results with the throat surface temperature from 2000 to 3250 [K] because the experiments did not measure or evaluate throat wall temperature. Most of the test results were distributed in the range of the calculation results between 2000 [K] to 2750 [K], which is a reasonable range of throat surface temperature. Our calculation results assuming constant wall temperatures showed smaller sensitivities to equivalence ratio than the test results. This is probably because the burn time was only a few seconds – not enough to reach a heat equilibrium so that the throat surface temperature increased over the test. This explanation is supported by the description in their paper [26] that all the tests started from the largest equivalence ratio and finished at the smallest equivalence ratio. This also explains the good agreement of the test results in the low equivalence ratios with the calculation results with high throat surface temperatures. This comparison showed that our simple model agreed well with the experimental results of nozzle throat erosion. In the flight simulations, we used the throat erosion model with the throat surface temperature of 3000 [K] to maximize the effect of throat erosion on performance.

IV.   Conceptual Design of Hybrid Sounding Rockets

Flight simulations require external dimensions of rockets to calculate aerodynamic drag. For launching rockets, the volumes of propulsion subsystems including propellant tanks dominantly affect the external dimensions. On the other hand, for hybrid rockets, the dimensions of the solid fuel grain strongly affect the maximum thrust-to-weight ratio because thrust is restricted by fuel port surface area and port cross-sectional area. In this section, a simple method is developed to calculate the external dimensions of the oxidizer tank and solid fuel grain satisfying the required aspect ratio of the propulsion subsystem and thrust-to-weight ratio.

A. Assumptions and Given Parameters

In this paper, we assume that the hybrid sounding rockets have a 2100 [kg] gross mass with a 100 [kg] payload. These specifications were intended to size rockets on the same scale as S-520 sounding rocket series, which have been the most often-launched type of sounding rockets in Japan, and its open specifications [27] enabled us to assume parameters to be given and compare the dimensions sized with S-520 series. The scaled-down rockets with one-third and one-ninth gross mass were also simulated to investigate the scaling effects of the factors dependent on O/F shifts

such as ideal propulsive performance, c^* efficiency, and throat erosion rate. The gross masses of these scaled-down rockets are similar to those of S-310 and S-210 Japanese sounding rockets [28], respectively.

Figure 5 shows the assumed configuration of the stored propellant. This paper does not consider the volumes of the payload or structures of the rocket because our one-dimensional flight simulation only requires the cross-sectional area of the rocket for the calculation of aerodynamic drag. Moreover, we also ignored the dimensions of the thickness of the motor case and oxidizer tank, and their dimensions were calculated only from the occupied volumes by the solid fuel, fuel port, and oxidizer stored in the liquid state. Pre- and post-chambers are important for high c^* efficiency in hybrid rocket propulsion, these components were also ignored in the conceptual design phase in this paper. This is also because their design criteria have not been established especially for swirling hybrids. Moreover, according to the investigation of swirling wax hybrids by Saito et al. [18], the fuel port volume gives a 6 times larger impact on c^* efficiency than the post-chamber volume due to the low velocity and long staying time of propellants in the fuel port. The outer radius of the solid fuel grain, r_{out}, was assumed to be equal to that of the oxidizer tank.

We selected paraffin wax and gaseous oxygen as the propellants, and the gaseous oxygen was assumed to be stored in the liquid phase. The liquid oxygen was assumed to be vaporized by any subsystems like a regeneratively-cooled nozzle [29], but the mass or volume of the vaporizing subsystem was not modeled here. The propellant mass ratio of 0.714 was assumed to simplify the conceptual design and common to all the rockets in this study, though this parameter actually depends on the maximum load in the flight and the dimensions of the rocket. The total aspect ratio including the fuel grain and the oxidizer tank was also assumed to range from 7 to 16. The aspect ratios of the solid rocket motor of S-520 is included in this range [28]. (The specifications of the motors in the other sounding rockets are not published by the Institute of Space and Astronautical Science, JAXA, but at least the rocket motor of S-310 has an aspect ratio in this range, estimating from the official schematics of S-310.) Initial port to throat diameter ratio, φ_{in}, and the maximum oxidizer mass flow rate, $G_{o\,max}$, are also important parameters which restrict initial thrust and filling rate of the solid fuel. Here we selected the constant φ_{in} of 2, which is a conservative value but enables us to ignore the gaseous velocity in the chamber for liquid propulsion [30]. We assumed $G_{o\,max}$= 350 [kg/m^{2}s] to prevent "flooding phenomena [3]", which refer to blowing out of the flame on the solid fuel. There were no detailed studies on these phenomena found, but G_o from 350 to 700 [kg/m^{2}s] is regarded as the upper limit of a practical design of hybrid rocket motors [3]. For the firing tests of the large-scale axial hybrids using paraffin and gaseous oxygen [9], the largest oxidizer mass flux was approximately 370 [kg/m^{2}s]. We assumed that the motor operates at the maximum oxidizer

mass flux, $G_{o\,max}$, at lift-off because it is known that the maximum thrust of the rocket at lift-off provides the highest altitude for the rocket [30]. The flight simulations were performed at the O/F ratios of the gross propellants from 1.6 to 2.1 by 0.1. For simplicity, in this design phase, the specific impulse of 280 [s] was assumed for all the simulations. This is the theoretical sea level specific impulse of paraffin wax and oxygen when O/F ratio is 2.0, the chamber pressure is 3 [MPa], and the nozzle expansion ratio of 5. This temporal value of 280 [s] was used only for the scaling of the thrust-to-weight ratio of the propulsion system at lift-off. The nozzle expansion ratio of 5 was selected to avoid nozzle flow separation at deep throttling.

B. Constraints to Dimensions of a Rocket

Next, the aspect ratio – including the oxidizer tank and the solid fuel grain – and the initial thrust-to-weight ratio were calculated using the given parameters and assumptions set in the above subsection.

Let us define solid fuel outer radius to throat radius ratio, $\varphi_{out} = r_{out}/r_t$, as well as φ_{in}. The initial mass of the solid fuel, m_{sf}, and the oxidizer, m_o, are expressed as

$$\begin{cases} m_{sf} = \pi \rho_{sf} (\varphi_{out}^2 - \varphi_{in}^2) r_t^2 L_{sf} \\ m_o = \rho_o \pi \varphi_{out}^2 r_t^2 L_o \end{cases} \tag{23}$$

where L_{sf}, L_o, ρ_{sf}, and ρ_o refer to the lengths of the solid fuel grain and the oxidizer tank and the densities of the solid fuel and the oxidizer, respectively. These variables and Eq. (3) provide the O/F ratio of the product gas at the lift-off $(O/F)_i$ as

$$\left(\frac{O}{F}\right)_i = \frac{\varphi_{in} r_t G_{o\,max}^{1-n_1}}{2\rho_{sf} a_0 (1+S_g^2)^{n_2} L_{sf}} \tag{24}$$

where the motor was assumed to operate at the oxidizer mass flux of $G_{o\,max}$. Eliminating L_{sf} in Eq. (24) with Eq. (23) enables us to express r_t with the three unknown variables φ_{out}, S_g, and $(O/F)_i$:

$$r_t = \left\{ \frac{2a_0(1+S_g^2)^{n_2} m_{sf}(O/F)_i}{\pi(\varphi_{out}^2 - \varphi_{in}^2)\varphi_{in} G_{o\,max}^{1-n_1}} \right\}^{\frac{1}{3}} \tag{25}.$$

When the O/F ratio of the gross propellants is assumed to be equal to $(O/F)_i$, Eqs. (23)-(25) provide the aspect ratio of the propulsion subsystem including the fuel grain and the oxidizer tank AR:

$$AR = \frac{L_{sf}+L_o}{2r_{out}} = \frac{\frac{\varphi_{in}}{\varphi_{out}} G_{o\,max}^{1-n_1}}{4\left(\frac{O}{F}\right)_i \rho_{sf} a_0 (1+S_g^2)^{n_2}} + \frac{\frac{\varphi_{in}}{\varphi_{out}}\left\{1-\left(\frac{\varphi_{in}}{\varphi_{out}}\right)^2\right\} G_{o\,max}^{1-n_1}}{4\rho_o a_0 (1+S_g^2)^{n_2}} \tag{26}.$$

This equation suggests that AR has the two degrees of freedom of $\varphi_{in}/\varphi_{out}$ and S_g under the given assumptions and parameters. These two variables also give the initial thrust-to-weight ratio $(F/W)_i$ and the density of the propellants averaged over the tank and the combustion chamber:

$$(F/W)_i = \frac{\pi G_{o\,max}\varphi_{in}^2\{1+(O/F)_i\}}{m_i(O/F)_i}r_t^2 I_{sp} = \frac{\pi^{\frac{1}{3}}I_{sp}\{1+(O/F)_i\}}{m_i(O/F)_i}\left\{2m_o a_0\left(1+S_g^2\right)^{n_s}G_{o\,max}^{\,n_o+\frac{1}{2}}\frac{\left(\frac{\varphi_{in}}{\varphi_{out}}\right)^2}{1-\left(\frac{\varphi_{in}}{\varphi_{out}}\right)^2}\right\}^{\frac{2}{3}} \tag{27}$$

$$\rho_{ave} = \frac{1+(O/F)_i\left\{1-\left(\frac{\varphi_{in}}{\varphi_{out}}\right)^2\right\}}{\frac{\rho_o}{\rho_{sf}}+(O/F)_i\left\{1-\left(\frac{\varphi_{in}}{\varphi_{out}}\right)^2\right\}}\rho_o \tag{28}$$

where m_i refers to the initial mass of the rocket, and I_{sp} was assumed to be 280 [s] as discussed in the previous subsection.

Figure 6 shows the relation among S_g, $(F/W)_i$, and AR for the total mass of 2100 [kg] and the gross propellant O/F of 2.0. The black curves show that there are two solutions of $\varphi_{in}/\varphi_{out}$ for an AR, but we only discuss the smaller solutions because the larger solution gives quite a small effective density. This figure also shows that S_g at the lift-off larger than 8 gives too small an AR for a sounding rocket. The maximum aspect ratio is 7.73 for $S_g = 8.0$ whereas the AR of S-520 is 10.3, but small S_g does not give controllability of regression rates against O/F shifts to the fuel-rich direction. Thus, we selected the dimensions of the rocket assuming $(S_g, (F/W)_i)=(6.0, 10)$. This assumption gave the AR from 6.2 to 9.1 for the three scales of sounding rockets. The dimensions and aspect ratios of the three scales of the rockets are shown in Figs. 7 a) and b). Figure 7 b) also shows the constant S_g of the O/F-uncontrolled types to consume both fuel and oxidizer at the engine cut-off. The method to calculate this parameter is explained in the next section.

V.   Flight Simulation

This section presents the flight dynamics model of rockets and the thrust control law necessary to calculate trajectories after defining the problem of the flight simulations. The actual block diagram of the flight simulation code and the calculation conditions of the rockets are also explained here.

A. Problem Setting

The objective of the flight simulation is to evaluate the effects of O/F shifts on flight performance under the nominal fuel regression behavior. This kind of O/F shift is expected to affect only the propulsive performance including the enthalpy of the productive gas, nozzle throat erosion, and c^* efficiency. We simulated 6 different gross

O/F cases from 1.6 to 2.1 for both O/F-controlled and -uncontrolled hybrid rockets. These two types of hybrid rockets are capable of thrust control. For the O/F-uncontrolled rockets, the program finds a constant geometric swirl number S_g to spend all fuel and oxidizer at the engine cut-off. This adjustment of S_g allows eliminating the effects of propellant residuals on flight performance. The flight simulations were performed for the three scales of rockets with the gross masses of 2100, 700, and 233 [kg] to evaluate the scale-effects on the performance loss due to O/F shifts. These three scales correspond to the Japanese sounding rocket series S-520 [27], S-310, and S-210 [28], respectively.

B. Ambient Conditions and Flight Dynamics Models

This simulation assumed one-dimensional vertical motions of a mass point representative of a rocket launched at sea level. Thus, gusts of wind or Coriolis force due to the spin of the earth was ignored here. Aerodynamic drag and gravity were assumed as the external forces exerted to the mass point. The International Standard Atmosphere (ISA) model [32] was used for the atmosphere model to calculate the ambient pressure. The constant standard gravity g of 9.80665 [m/s^2] at sea level was used for the gravity model. The magnitude of the gravity is important to determine the target throttling ratio but gravity models precise to the altitude direction are not essential for this simulation because the altitude during the powered flight was less than 50 [km], corresponding to less than 1.6% increase from the universal gravitation model. For the aerodynamic drag model, we used a simple drag model proposed by Akiba et al. [33].

C. Thrust and Mixture Ratio Control

In the flight simulations, the thrust was controlled to increase the altitude, but re-ignition of the engine was not accepted as most single-stage sounding rockets do not have such capability. This thrust control is also intended to evaluate the effects of O/F shifts in deep throttling on the nominal propulsive performance of hybrid rockets.

The problem setting of our simulations is quite similar to that of the Goddard problem [34]. In the idealized Goddard problem with a constant specific impulse and the throttle ratio from zero to the maximum, it is easy to find the candidates of the optimal control law: bang-bang control and throttling to maintain a singular surface, however, the retrieval of the global solution is significantly difficult due to the practically infinite combinations of these candidates [31].

On the other hand, we have a complicated problem setting that there is a lower limit of throttling and a shift in specific impulse. The lower throttling limit depends on O/F ratio and ambient pressure to avoid nozzle flow separation,

and the specific impulse depends on propellant mass flow rate, O/F ratio, and ambient pressure mainly due to the character of the divergent nozzle. This lower limit of throttling should be the lower part of the bang-bang control in our problem setting, however, the latter condition provides a large complexity for the problem because the dependence of the specific impulse on the state variables eventually require the consideration of the rate of throttling in addition to the matrix of second-order partial differentials of specific impulse for the calculation of the throttling maintaining the singular surface. For simplicity, our simulations use the control law maintaining the singular surface assuming a constant specific impulse to avoid the difficulty in solving this complicated problem. This control law also gives far better performance than the constant 100% throttling ratio and is useful to evaluate the effects of O/F shifts in the thrust curve including deep throttling.

Our throttling law that we applied uses a function of state vector $f(x)$ to evaluate whether the state vector is above, on, or beneath the singular surface assuming a constant specific impulse:

$$f(x) = 1 + \frac{D(x,v)}{mg} - \frac{D(x,v)v}{mg^2 I_{sp}} - \frac{\partial D(x,v)}{\partial v} \frac{v}{mg} \tag{29}$$

where $x = (x, v, m)^{\mathrm{T}}$.

The control law is as follows:

$$\dot{m} = \begin{cases} \dot{m}_{\max} & (f(x) > \delta) \\ \dot{m}_{\min} & (f(x) < -\delta) \\ \dot{m}_{\mathrm{mid}} & (|f(x)| \leq \delta) \end{cases} \tag{30}$$

where $\delta = 10^{-3}$. $\dot{m}_{\mathrm{mid}}$ is determined as

$$\dot{m}_{\mathrm{mid}} = \begin{cases} \dot{m}_s & (\dot{m}_{\min} \leq \dot{m}_s \leq \dot{m}_{\max}) \\ \dot{m}_{\min} & (\dot{m}_s < \dot{m}_{\min}) \\ \dot{m}_{\max} & (\dot{m}_s > \dot{m}_{\max}) \end{cases} \tag{31}$$

$\dot{m}_s$ is calculated by the following equation:

$$\dot{m}_s(x) = \frac{\left(D + mg - v\frac{\partial D}{\partial v}\right)}{vD} \frac{(D+mg)\left\{\left(D+mg-v\frac{\partial D}{\partial v}\right)\left(D+v\frac{\partial D}{\partial v}\right) + v^2 D\frac{\partial^2 D}{\partial v^2}\right\} - mv^2\left\{\left(mg-v\frac{\partial D}{\partial v}\right)\frac{\partial D}{\partial x} + vD\frac{\partial^2 D}{\partial x \partial v}\right\}}{(D+mg)^2 - \left(v\frac{\partial D}{\partial v}\right)^2 + v^2 D\frac{\partial^2 D}{\partial v^2}} \tag{32}.$$

The details of the derivation and validation of the control law are discussed in Appendix A. We should note that this control law cannot actually keep the state vector on the singular surface even if the thrust is controlled along with 3) (a) because the specific impulse is not constant during the flight. In the actual flight simulation code, once the rocket operates with the control law 3) (a), $f(x)$ is not updated in the following time step until $\dot{m}(x)$ fulfills the condition

$\dot{m}_{\min} \le \dot{m}(\boldsymbol{x}) \le \dot{m}_{\max}$. $\dot{m}_{\min}$ is determined as the mass flow rate satisfying the threshold of the nozzle flow separation [35]:

$$\frac{p_{e_{\text{sep}}}}{p_a} = \frac{2}{3}\left(\frac{p_{c_{\text{sep}}}}{p_a}\right)^{-\frac{1}{5}} \tag{33}$$

where $p_{c\,\text{sep}}$ and $p_{e\,\text{sep}}$ refer to chamber and nozzle exit pressures at the mass flow rate on the separation limit $\dot{m}_{\min}$, respectively.

For the O/F-controlled cases, O/F shifts are eliminated or compensated for by changing geometric swirl number S_g. The target S_g is analytically calculated from Eq. (2) as

$$S_g^2 = \left\{\frac{r_p^{2n_1-1}}{\pi^{1-n_1}a_0\rho_f L(O/F)}\dot{m}_o^{1-n_1}\right\}^{\frac{1}{n_2}} - 1 \tag{34}$$

where S_g^2 should be a positive value or zero. When Eq. (34) gives a negative S_g^2, the code returns $S_g^2 = 0$, and the O/F shift is reduced but not eliminated. $S_g^2 < 0$ means the O/F shift exceeded the capability of the O/F shift elimination using swirling oxidizer injection. S_g actually has an upper limit dependent on the design of the swirling injector and the performance of the oxidizer supply, and it is around 30 to 50 for gaseous oxygen [36] if the injector does not accept choking. However, our code did not assume such an upper limit because such a large S_g was not required in our simulations.

D. Block Diagram of Simulation Program

Figure 8 shows the block diagram of the flight simulation code. At the beginning of the simulation, the program calculates the dimensions of the rocket from the gross O/F ratio of the propellants and the other design parameters. The maximum oxidizer mass flow rate is also determined here from the initial port diameter and the maximum oxidizer mass flux.

At the start of each time step, the code checks that both oxidizer and fuel remain in the rocket. If so, the engine operates and outputs thrust, the program calculates the throttle range from the altitude of the rocket. The program determines the target throttle ratio using the $f(\boldsymbol{x})$ at the last time step and the thrust control law. If the engine was controlled along with 3) (a) in the last time step, the program continues the throttling with $\dot{m} = \dot{m}_s$ along with 3) (a) without calculating $f(\boldsymbol{x})$ at that time step as long as the $\dot{m}$ satisfies $\dot{m}_{\min} \le \dot{m}(\boldsymbol{x}) \le \dot{m}_{\max}$. Otherwise, the program outputs the target mass flow rate subject to the thrust control law. If the remaining propellants are smaller than the target throttle, then they are completely used in that time step.

Once the target mass flow rate is determined, the program calculates the engine performance and nozzle throat erosion rate that are used for the step of the time-integration. The ideal chamber pressure is calculated by the iteration comparing the result of the Gibbs Energy minimization under the enthalpy-pressure problem [12] and the choking condition at the nozzle throat with the calculated mass flow rate. The ideal chamber pressure is calculated from the actual chamber pressure and c^* efficiency Eq. (14). The throat erosion rate is calculated using Eqs. (15), (17), (21), and (22). The boundary condition of the mole fraction at the core flow x_{i0} is calculated from the Gibbs Energy minimization with the product gas. In this calculation, the $a_t^2/2$ is assumed to be used for the specific kinetic energy from the specific total energy of the product gas. When the O/F control is activated for the O/F-controlled rockets, Eq. (34) calculating S_g is also included in the iteration to match the O/F ratio of the gas flow in the combustion chamber with that of the propellants remaining in the rocket at that time step.

In the final part of the time step, the state vector is updated by the time-integration of the following equation of motion with the fourth-order Runge-Kutta method:

$$\begin{cases} \frac{dx}{dt} = v \\ \frac{dv}{dt} = F/m - D(x,v)/m - g \\ \frac{dm}{dt} = -\dot{m} = -\dot{m}_o - \dot{m}_f \end{cases} \tag{35}.$$

The remaining mass of the oxidizer, the port diameter of the fuel grain, and the throat diameter are also updated with the Euler method for simplicity and computing time. These time-integrations are carried out with the time interval of 0.01 [s]. At the end of each time step, the function Eq. (29) is updated using the instantaneous specific impulse at that time step for the following time step.

The powered flight continues until either the fuel or oxidizer is spent out. After the engine cut-off, the free flight continues until the velocity becomes negative. For the O/F-uncontrolled cases, the constant geometric swirl number was retrieved to spend both fuel and oxidizer out simultaneously at the engine cut-off.

VI.   Results and Discussion

Figures 9 a) and b) show the apogee above sea level and the specific impulse averaged over the powered flight, respectively. The O/F-controlled type performed better than the O/F-uncontrolled type for all the conditions. Both types achieved the best performance in specific impulse with all scales for O/F = 1.9, whereas they reached the highest apogee at the O/F ratios of 1.8, 1.8, and 1.9 for the gross mass of 233, 700, and 2100 [kg], respectively. The best case in apogee above sea level was the O/F-controlled type with the gross mass of 2100 [kg] and the propellant O/F ratio

of 1.9, and the rocket reached 254.9[km] altitude and its averaged specific impulse was 226.8[s]. However, the performance improvement from the O/F-uncontrolled type was relatively small. The increase ratios in apogee and specific impulse ranged from 4.21% to 8.10% and from 1.95% to 2.44%, respectively. For the gross mass of 233 [kg], the O/F-controlled type resulted in the averaged specific impulse of 223.8 [s] for O/F = 1.9 and the apogee of 213.8 [km] above sea level for O/F = 1.8 while that for the gross mass of 700 [kg] did in 219.0 [s] and 155.1 [km], respectively. The detailed summary of the results is shown in Table 1.

A. Time-trace of Results

The differences in the performance of the two types with the gross mass of 2100 [kg] and the gross propellant O/F ratio of 1.9 are compared in Figs 10–11. Figure 10 shows the time traces of altitude, velocity, and acceleration over the calculations. These three curves of the two types were quite similar to each other, but the O/F-controlled rocket reached a higher altitude than O/F-uncontrolled due to the effective use of the propulsive performance. The burn time for the O/F-controlled type was shorter than O/F-uncontrolled type and took the longer coasting time to apogee. These trends were observed in all the cases simulated.

Figure 11 a) shows the time-traces of propellant mass flow rate and geometric swirl number. The initial thrust of the O/F-controlled type was larger than that of the O/F–uncontrolled type because of the lower fuel mass flow rates of the latter type with the constant S_g of 3.69. This smaller thrust delayed the throttling operation for 0.82 [s]. The state vector of the O/F-controlled type reached the singular surface at 7.06 [s], but the minimum thrust larger than $\dot{m}_s$ was selected due to the nozzle flow separation limit. The state vector reached on the singular surface again at 19.41 [s], and the throttle ratio of $\dot{m}_s$ was selected, and finally, the singular surface was maintained until the engine cut-off. The deepest throttle ratio was 18.4 [%] for the O/F-controlled type compared to 15.2 [%] for the O/F-uncontrolled type. For the O/F-controlled type, the geometric swirl number ranged from 0.58 to 7.31, and the instant O/F was kept constant.

Figure 11 b) shows the time traces of throat area expansion ratio, instantaneous O/F ratio, and c^* efficiency. O/F ratio was maintained over the engine operation for the O/F-controlled type but shifted from 1.22 to 2.33 for the O/F-uncontrolled type. At the beginning of the launch, O/F shifts occurred to the oxidizer-rich direction due to the low fuel regression rates and caused throat erosion rates larger than the O/F-controlled type. Conversely, the deep throttling caused O/F shifts toward the fuel-rich direction, leading to lower throat erosion rate than the O/F-controlled type in the middle of the engine operation. At the end of the powered flight of the O/F-uncontrolled type, the O/F ratio and

erosion rate were higher than those of the O/F-controlled due to the shallow throttle ratios. Consequently, the O/F-controlled type had a total throat erosion slightly larger than the O/F-uncontrolled type. This result is explained by the slightly larger total impulse and enthalpy of the product gas from the O/F-controlled type. However, the O/F-controlled type showed the smaller throat expansion ratio averaged by the propellant mass flow rate (3.72 [%]) than the O/F-uncontrolled type (4.06 [%]). These results suggest that the O/F-controlled type had a larger total erosion but prevented the erosion at the large throttle ratios, resulting in the small I_{sp} loss. The c^* efficiency changed from 83.0 to 88.4 [%] according to S_g for the O/F-controlled type but stayed near to the constant value of 85.5 [%] for O/F-uncontrolled type over the engine operation for the best cases of the gross mass of 2100 [kg]. This complicated result is due to many factors affecting c^* efficiency: instantaneous throat area, fuel port volume, propellant mass flow rate, and O/F ratio. These results suggest that $\bar{L}^*$ was large enough for diffusion over the burns in both cases so that the dominant factor to determine c^* efficiency has become S_g. The weight-averaged c^* efficiency by propellant mass flow rate was 85.9 [%] and 85.5 [%] for O/F-controlled and –uncontrolled types, respectively, therefore, the difference in c^* efficiency was also small between the two types of rockets with the scale of S-520. The performance increase in I_{sp} among enthalpy of the product gas, throat erosion, and c^* efficiency is analyzed in more detail in the following subsection C.

B. Scale Effects of Performance

Scale effects were observed in the performance improvements to some degree. The largest performance increase by the O/F control depended on the scale of rockets: 7.11% in the highest altitude and 2.42% in specific impulse for 233 [kg]; but 4.69% in the highest altitude and 2.04% in specific impulse for 2100 [kg]. This difference should have correlations with the scale effects of theoretical I_{sp}, c^* efficiency, and throat erosion. However, in this subsection, we only discuss those of the latter two performance factors, and their influence on I_{sp} are discussed in the following subsection as well as the theoretical I_{sp} increase because the share estimation of performance increase is needed to reveal each contribution.

The scale effect of throat erosion was considerable in the two factors. This is because the throat erosion rate and engine operating time were of the same order of magnitude in all the scales so that the nozzle throat expansion ratio at the engine cut-off increased with decreasing the scale of rockets. For example, for the O/F-controlled type with the gross mass of 233 [kg], the throat expansion ratio ranged from 19.7 to 32.6% versus 5.23 to 8.88% for 2100 [kg]. Figure 12 a) shows the throat area increase ratio for all the cases simulated. The O/F-controlled type had slightly larger

throat erosion for all the cases compared to the O/F-uncontrolled type, but the difference in throat area expansion was less than 0.96%. The largest case was for the gross mass of 233 [kg] and the O/F ratio of 2.1.

On the other hand, the scale effect on the weight-averaged c^* efficiency by propellant mass flow rate was very small as shown in Fig. 12 b). The O/F-uncontrolled type had the larger difference in the weight-averaged c^* efficiency between the gross masses of 2100 and 233 [kg], but it was less than 0.15 [%]. The difference between the two types was rather large, but it was also at most 0.44 [%]. Therefore, c^* efficiency was mainly improved by the O/F control, and the increase of L^* was secondly effective and negligible among these three scales.

C. Share Estimation of Increase in Specific Impulse

Here, we estimated the improvement in the ideal specific impulse due to the shifts in unit mass enthalpy of the product gas and the shares of the loss in specific impulse between c^* efficiency and nozzle throat erosion. These shares were analyzed by combining the rocket engine performance evaluation program with the resultant data of the flight simulations: the time histories of the state vector, c^* efficiency, throat area. We calculated three time-averaged specific impulses along with the time history of the resultant state vector with the following different conditions of c^* efficiency and throat area: 1) 100% c^* efficiency and no throat erosion, 2) c^* efficiency history of the flight simulation and no throat erosion, and 3) 100% c^* efficiency and throat erosion history of the flight simulation. We used these three calculations to separately evaluate the factors affecting the performance. The case 1) was used for the comparison of the ideal performance between O/F-controlled and –uncontrolled types, and all three cases were used for the share estimation of the c^* efficiency and throat erosion in the I_{sp} loss from the ideal time-averaged I_{sp}. The simulation result is approximated to first-order accuracy by the following equation using the three cases:

$$\overline{I_{sp}}(\eta_{c^*}, A_t) = \frac{\int_{t_i}^{t_f} F\left(x, \eta_{c^*}(t), A_t(t)\right) dt}{m_o + m_{sf}} = \frac{\int_{t_i}^{t_f} \left\{F(x, \eta_{c^*}, A_{t_i}) + F(x, 1, A_t) - F(x, 1, A_{t_i}) + O\left(\delta^2(\eta_{c^*}) + \delta^2(A_t)\right)\right\} dt}{m_o + m_{sf}}$$

$$\approx \overline{I_{sp}}(1, A_{t_i}) - \left(\overline{I_{sp}}(1, A_{t_i}) - \overline{I_{sp}}(\eta_{c^*}, A_{t_i})\right) - \left(\overline{I_{sp}}(1, A_{t_i}) - \overline{I_{sp}}(1, A_t)\right) \quad (36)$$

where $\overline{I_{sp}}$ refers to time-averaged specific impulse, and thrust was regarded as a function of time traces of state vector, c^* efficiency, and nozzle throat area. The two terms $\left(\overline{I_{sp}}(1, A_{t_i}) - \overline{I_{sp}}(\eta_{c^*}, A_{t_i})\right)$ and $\left(\overline{I_{sp}}(1, A_{t_i}) - \overline{I_{sp}}(1, A_t)\right)$ refer to the I_{sp} losses due to throat erosion and c^* efficiency, respectively.

Figure 13 a) shows the comparison of the ideal time-averaged specific impulse with the performance losses due to throat erosion and c* efficiency for the best cases in averaged specific impulse. The first-order approximation of the

time-averaged I_{sp} using Eq. (36) had agreements with the flight simulation results within the 0.15-point error, enabling us to evaluate the effects of c^* efficiency and throat erosion separately. The increase ratios of the O/F control were 1.38, 1.34, and 1.30 [%] for the gross masses of 233, 700, and 2100 [kg], respectively. This figure shows that the improvement of the unit mass enthalpy of product gas gives 1.3-1.4% increase in the ideal time-averaged I_{sp} with a small dependence on the scale. This trend is caused by the following mechanism: 1) the smaller the scale of the rocket is, the smaller the aspect ratio is; 2) the smaller aspect ratio causes the larger throttle range and O/F shifts for O/F-uncontrolled types; 3) ultimately, with decreasing the scale, O/F-uncontrolled types lose the time-averaged specific impulse by more percent. Moreover, this trend should be influenced also by the averaged ambient pressure under which the engine operated. This parameter affecting the nozzle performance also depends on the aspect ratio and aerodynamic drag.

Figure 13 a) also shows the results of the share estimation of c^* efficiency and throat erosion in the I_{sp} loss for both types. The I_{sp} loss of c^* efficiency was dominant in these two factors for all cases analyzed, but its scale effects were negligible – less than 0.4 [%] compared to the scale of the I_{sp} loss. The corresponding I_{sp} loss was 16.1 to 16.4 [%] and 16.7 to 17.1 [%] for O/F-controlled and –uncontrolled types. The I_{sp} loss fraction of throat erosion was negligible, but small-scale effects were observed there as well as in the ideal time-averaged I_{sp} due to the difference of L^*. The smaller L^* resulted in large I_{sp} losses of 1.43% and 1.56% for the O/F-controlled and -uncontrolled types with the gross mass of 233 [kg], respectively, and the I_{sp} loss for 2100 [kg] was improved down to 0.39 and 0.41 [%], respectively.

Figure 13 b) shows the contribution of the improvement in the time-averaged I_{sp} by adopting the O/F control. The total increase was 5.18, 4.78, and 4.54 [s] for the gross masses of 233, 700, and 2100 [kg]. This improvement is mainly from ideal specific impulse (3.62, 3.57, and 3.49 [s], respectively), secondly from c^* efficiency (1.25, 1.09, and 0.990 [s], respectively), and that of throat erosion gave negligible improvements of 0.298, 0.121, and 0.0551 [s], respectively. In the total increase of I_{sp}, the improvement of theoretical I_{sp} had the largest share from 70.0 to 77.0 [%], and it should be noted that the improvement of c^* efficiency also had a significant share of 21.8 to 24.3 [%] in the whole I_{sp} increase. However, a detailed discussion is needed on the impact of c^* efficiency in the future because this improvement is unique to the O/F control with swirling injection, and its share decreased with increasing the scale of rockets. Moreover, practically, well-designed post-chambers with any mixing enhancer like baffle plates may enable high c^* efficiency

near to 100 [%]. Throat erosion had a barely meaningful 5.75 [%] contribution to the I_{sp} increase for the smallest scale, but the share was down to 1.21 [%] for 2100 [kg], a negligible impact due to its scale effect.

Therefore, we can conclude that O/F control applying swirling injection gives 2.04 to 2.42 [%] increase in the time-average I_{sp} in the scale of rockets from S-210 to S-520 series mainly due to the improvement of the unit mass enthalpy of the product gas and c^* efficiency. The contributions of these factors are approximately 70 to 77 [%] and 22 to 24 [%], and the throat erosion had a very small contribution of less than 6% only for the smallest scale of S-210.

VII.   Conclusions

This paper evaluated the improvement of flight performance by applying the O/F-controlled hybrid propulsion for single-stage sounding rockets as a complex practical problem of hybrid rocket propulsion, assuming the nominal fuel regression behavior. The flight simulations included the calculation models of the three factors affected by O/F shifts. The two of them, c^* efficiency and throat erosion, were validated with experimental results.

The flight simulations were performed for the O/F-controlled and –uncontrolled types with the three scales of the gross mass and the propellant O/F ratio ranging from 1.6 to 2.1. The O/F-controlled rockets performed better than the O/F-uncontrolled rockets both in specific impulse and apogee for all the conditions. The differences between the two types were from 1.95 to 2.44 [%] in specific impulse and from 4.21 to 8.10 [%] in the highest altitude, respectively. The performance improvement slightly decreased with increasing the scale of rockets mainly due to the improvements of the ideal specific impulse, c^* efficiency, and throat erosion of the O/F-uncontrolled type. The O/F-controlled type had the larger weight-averaged c^* efficiency by propellant mass flow rates than the O/F-uncontrolled type, not due to the increase of $\bar{L}^*$ but due to large S_g in high throttling operations. The final throat area of the O/F-controlled type was larger than that of O/F-uncontrolled type for all cases, but the O/F control gave the smaller weight-averaged throat area.

Scale effects were observed in throat erosion but negligible for c^* efficiency. The total throat expansion ratio for the O/F-controlled hybrid rockets with the scale of S-210 was 14.2-23.8 % larger than that for the scale of S-520 because the scale of throat erosion rates did not depend on the scale of rockets. The differences of the weight-averaged c^* efficiency by propellant mass flow rates were less than ±0.15 [%] between the scales of S-210 and S-520 because L^* was large enough for the sufficient staying time.

For the scale of S-210, approximately 70% of the total performance improvement was attributed to the elimination of enthalpy shifts, and 24% was due to the improvement of c^* efficiency. The remaining improvement was the contribution of the improvement of throat erosion, but it was less than 0.3 [s] in specific impulse. With increasing the scale, the contribution of the elimination of enthalpy shifts to the I_{sp} improvement increased, and its share became approximately 77 [%] for 2100 [kg]. The contribution of c^* efficiency improvement was secondarily significant up to approximately 24 [%] but slightly decreased the share with increasing the scale down to approximately 22 [%] for 2100 [kg]. However, the implementation of mixing enhancers like baffle plates may eliminate such large contributions of c^* efficiency improvement because the improvements observed in the simulations were mainly due to the use of strong swirl in large throttling operations of O/F-controlled rockets. The contribution of throat erosion improvement to I_{sp} improvement was negligible -- less than 5.5 [%] -- corresponding to the increase by 0.298 [s] in this range of the scale.

As a conclusion, this paper clarified that O/F control in hybrid rocket propulsion improves the flight performance of sounding rockets by 1.2 to 2.7% in the averaged specific impulse for the median fuel regression behavior without any uncertainty in fuel regression. These small performance increases can be canceled out by the increase in the structural mass of a more complex oxidizer feed system of O/F-controlled hybrid rockets.

However, the performance shown in this paper is the best case not considering the statistical uncertainty in the fuel regression, and this assumption allows neglecting the effects of residual propellants. In order to evaluate the effects of O/F shifts due to the uncertainty in fuel regression, some statistical or random error models should be applied to the fuel regression behavior. This problem should be an important future topic in the field of hybrid rocket propulsion.

Appendix A: Validation of Thrust Control Law

This appendix presents the derivation of the thrust control law used in the flight simulations. As discussed in Section VI, for the simplicity of the derivation, the thrust control law was modelled from an idealized Goddard problem: a) specific impulse is constant; b) re-ignition is not accepted; and c) throttling ratio has lower and upper limits, and the lower limit depends on the ambient pressure. The difference in this problem from the Goddard problem typically discussed is whether throttling range has a lower limit or not. The following three candidates of the optimal thrust are derived by applying Pontryagin's maximum principle for this problem as in that without the lower limit of thrust [30] using the state vector $\boldsymbol{x} = (x_1, x_2, x_3)^{\mathrm{T}} = (x, v, m)^{\mathrm{T}}$ and its adjoint vector $\boldsymbol{\lambda} = (\lambda_1, \lambda_2, \lambda_3)^T$: 1) when $\lambda_3 -$

$I_{sp}g\lambda_2 > 0$, $\dot{m} = \dot{m}_{max}$; when $\lambda_3 - I_{sp}g\lambda_2 < 0$, $\dot{m} = 0$; when $\lambda_3 - I_{sp}g\lambda_2 = 0$, $\dot{m} = \dot{m}_s$. $\dot{m}_s$ should be selected to satisfy

$$x_2\left(I_{sp}g\frac{\partial D}{\partial x_2} + D\right) - I_{sp}g(D + x_3 g) = 0 \tag{37}.$$

The candidates of thrust 1) and 2) correspond to the bang-bang controls, and the other candidate 3) is called as a control on a "singular arc" or "singular surface" because the condition of 3) eliminates the control variable (propellant mass flow rate) from the Hamiltonian of this problem, and Eq. (37) describes a surface in the space of the state vector. Though we easily found the above candidates of the optimal control, it is practically impossible to analytically find the optimum control and the concrete adjoint vector because either initial or terminal boundary condition is indefinite for all the elements of the state and adjoint vectors. Moreover, there are infinite combinations of the control options 1) to 3). In these infinite candidates, Ben-Asher [30] recommends to check the performance of plausible control programs of $\{\dot{m}_{max} - 0\}$, $\{\dot{m}_{max} - \dot{m}_s - 0\}$, $\{\dot{m}_{max} - \dot{m}_s - \dot{m}_{max} - 0\}$, $\{\dot{m}_{max} - \dot{m}_s - \dot{m}_{max} - \dot{m}_s - 0\}$, ... in increasing order of complexity for the Goddard problem with the throttling range from zero to the maximum.

For our problem with the lower limit of throttling, the constraint of throttling is expressed as

$$\begin{cases} \dot{m}_{min}(x,m) \le \dot{m} \le \dot{m}_{max}(m) \\ m = m_{fin} \rightarrow \dot{m}_{max} = \dot{m}_{min} = 0 \\ m > m_{fin} \rightarrow \dot{m}_{min} = \dot{m}_{sep}(x), \dot{m}_{max} = \dot{m}_0 \end{cases} \tag{38}$$

where $\dot{m}_{sep}(x)$ and $\dot{m}_0$ refers to the minimum propellant mass flow rate not to cause the nozzle flow separation at an altitude x and a given maximum mass flow rate, respectively. Therefore, the candidates of the optimum thrust control are replaced by 1) $\dot{m} = \dot{m}_{max}$, 2) $\dot{m} = \dot{m}_{min}$, and 3) $\dot{m} = \dot{m}_s$. In our problem, the existence of $\dot{m}_{min}$ increased the candidates of thrust control laws. According to the discussion of the optimal control for a Goddard problem [37] with a complex aerodynamic drag model around the transonic region, sometimes $\dot{m}_s$ becomes negative when the state vector reaches the singular surface. For these cases, Tsiotras et al. [37] found control laws to leave the singular surface at that moment and select a bang-bang control, to reach the singular surface again as quickly as possible, and to stay on the singular surface under a given throttling constraint.

Here, we also compared the performance of the candidates to find the best control law under the constant specific impulse of 260 [s]. The candidates were the following two simple control laws: a) $\{\dot{m}_{max} - \dot{m}_s - \dot{m}_{max} - 0\}$; b) $\{\dot{m}_{max} - \dot{m}_{min} - \dot{m}_s - \dot{m}_{max} - 0\}$. The second $\dot{m}_{max}$ in both control laws is used when the calculated $\dot{m}_s$ is larger than $\dot{m}_{max}$. The thrust control law was switched in the following way using a threshold parameter $\delta = 10^{-3}$ and Eq.

(29), which is Eq. (37) normalized by $-mg^2 I_{sp}$: 1) when $f(\boldsymbol{x}) > \delta$, the rocket operates at $\dot{m} = \dot{m}_{max}$; 2) when $f(\boldsymbol{x}) <$ $-\delta$, the rocket operates at $\dot{m} = \dot{m}_{max}$ (control law a)) or $\dot{m} = \dot{m}_{min}$ (control law b)); 3) when $|f(\boldsymbol{x})| \leq \delta$, the controller checks whether $\dot{m}_s$ is in the throttle range, and when $\dot{m}_s > \dot{m}_{max}, \dot{m} = \dot{m}_{max}$, when $\dot{m}_s < \dot{m}_{min}, \dot{m} =$ $\dot{m}_{max}$ (control law a)) or $\dot{m} = \dot{m}_{min}$ (control law b)), and otherwise, $\dot{m} = \dot{m}_s$. The following minimum throttling ratio used in the validation was modeled by approximating the resultant flow separation limit in the flight simulation with the gross mass of 2100 [kg] and the propellant O/F ratio of 1.9:

$$\frac{\dot{m}_{min}}{\dot{m}_{max}} = -3.471 \times 10^{-2} x + 0.4966 \tag{39}$$

where x refers to an altitude of the rocket in km less than 14.31 [km]. For x larger than 14.31 [km], $\dot{m}_{min} = 0$. We assumed that the rocket had the diameter of 656 [mm] and the gross and final masses of 2100 [kg] and 609 [kg], respectively, and it was launched with the initial acceleration of 78.5 [m/s^2] at the maximum throttling ratio. These initial conditions are similar to those of the flight simulations for the gross mass of 2100 [kg] and the propellant O/F ratio of 1.9.

Figure 14 shows the time traces of the throttling ratio and switching parameter of the two control laws. For control law a), the state vector could not stay on the singular surface when it reached there at 7.75 [s] so that throttling ratio continued to be 100% whereas the state vector successfully reached again and stayed on the singular surface from 13.88 [s] to the end of the burn for control law b). The apogees were 310.1 [km] above sea level for a) and 339.7 [km] for b), respectively. This comparison has demonstrated the superiority of control law b) when the lower limit of throttling exists, therefore, we applied control law b) for the flight simulations.

References

[1] Ordahl, D. D., "Recent Developments and Current Status of Hybrid Rocket Propulsion," *Journal of Spacecraft and Rockets*, Vol. 2, No. 6, Nov. 1965, pp. 923–926.

doi: 10.2514/3.28315

[2] Waidmann, W., "Thrust Modulation in Hybrid Rocket Engines," *Journal of Propulsion and Power*, Vol. 4, No. 5, Sept.-Oct., 1988, pp. 421–427.

doi: 10.2514/3.23083

[3] Humble, R. W., Henry, G. N., and Larson, W. J., *Space Propulsion Analysis and Design*, McGraw-Hill, New York, 1995, Chap. 7.

doi: 10.1036/0070313202

[4] Barato, F., Grosse, M., Bettella, A., "Hybrid Rocket Residuals - An Overlooked Topic," *50th AIAA/ASME/SAE/ASEE Joint Propulsion Conference & Exhibit*, AIAA, Cleveland, Ohio, 2014, AIAA 2014-3753.

doi: 10.2514/6.2014-3753

[5] Ozawa, K., Kitagawa, K., Aso, S., and Shimada, T., "Hybrid Rocket Firing Experiments at Various Axial–Tangential Oxidizer-Flow-Rate Ratios," *Journal of Propulsion and Power*, Vol. 35, No. 1, Jan. 2019, pp. 94–108.

doi: 10.2514/1.B36889

[6] Shimada, T., Yuasa, S., Nagata, H., Aso, S., Nakagawa, I., Sawada, K., Hori, K., Kanazaki, M., Chiba, K., Sakurai, T., Morita, T., Kitagawa, K., Wada, Y., Nakata, D., Motoe, M., Funami,Y., Ozawa, K., Usuki, T., "Hybrid Propulsion Technology Development in Japan for Economic Space Launch," edited by L., De Luca, T., Shimada, V., P., Sinditskii, and M. Calabro, *Chemical Rocket Propulsion: A Comprehensive Survey of Energetic Materials*, Springer Aerospace Technology, Springer International Publishing, Cham, Switzerland, 2017, pp. 545-575.

doi: 10.1007/978-3-319-27748-6

[7] Shinohara, K., and Nakagawa, I., "Regression Rate Characteristics of Paraffin-based Fuel under Swirled Oxidizer Flow," *48th AIAA/ASME/SAE/ASEE Joint Propulsion Conference & Exhibit*, AIAA, Atlanta, Georgia, 2012, AIAA 2012-4104.

doi: 10.2514/6.2012-4104

[8] Saito, D., Yuasa, S., Hirata, K., Sakurai, T., and Shiraishi, N., "Combustion Characteristics of Paraffin-Fueled Swirling Oxidizer-Flow-Type Hybrid Rocket Engines," *48th AIAA/ASME/SAE/ASEE Joint Propulsion Conference & Exhibit*, AIAA, Atlanta, Georgia, 2012, AIAA 2012-3904.

doi: 10.2514/6.2012-3904

[9] Karabeyoglu, M., A., Zilliac, G., Cantwell, B., J., Zilwa, S., D., and Castellucci, P., "Scale-up Tests of High Regression Rate Liquefying Hybrid Rocket Fuels," *Journal of Propulsion and Power*, Vol. 20, No. 6, Nov.-Dec., 2004, pp. 1037-1045.

doi: 10.2514/1.3340

[10] Tamura, T., Yuasa, S., and Yamamoto K., "Effects of Swirling Oxidizer Flow on Fuel Regression Rate of Hybrid Rockets," *35th AIAA/ASME/SAE/ASEE Joint Propulsion Conference and Exhibit*, AIAA, Los Angeles, California, 1999, AIAA 99-2323.

doi: 10.2514/6.1999-2323

[11] Ross, S. M., *Introduction to Probability and Statistics for Engineers and Scientists*, 4th ed., Elsevier Academic Press, Massachusetts, 2009, Chap. 9.

[12] Gordon, S., and McBride, J. B., "Computer Program for Calculation of Complex Chemical Equilibrium Compositions and Applications," NASA Reference Publication 1311, 1994.

[13] NASA CEA, NASA Chemical Equilibrium with Applications, Software Package, Ver. May 21, 2004, NASA Glenn Research Center, Cleveland, OH, 2004.

[14] Zehe, M., J., Gordon, S., and McBride, J. B., "CAP: A Computer Code for Generating Tabular Thermodynamic Functions from NASA Lewis Coefficients," NASA TP 2001-210959/REV1, 2002.

[15] Huzel, D. K., and Huang, D. H. (ed.), *Modern Engineering for Design of Liquid-Propellant Rocket Engines*, AIAA, Washington DC, 1992, Chap. 4.

doi: 5.9781600866197.0067.0134

[16] Karabeyoglu, M., A. "Combustion Instability and Transient Behavior in Hybrid Rocket Motors," Fundamentals of Hybrid Rocket Combustion and Propulsion, edited by M. J. Chiaverini, and K. K. Kuo, Progress in Astronautics and Aeronautics, AIAA, Reston, 2007, pp. 351–411.

doi: 10.2514/5.9781600866876.0351.0412

[17] Ishiguro, T., Shinohara, K., Sakio, K., and Nakagawa I., "Combustion Efficiency of Paraffin-based Hybrid Rockets," *47th AIAA/ASME/SAE/ASEE Joint Propulsion Conference & Exhibit*, AIAA, San Diego, California, 2011, AIAA 2011-5679.

doi: 10.2514/6.2011-5679

[18] Saito, D., Yuasa, D., Sakurai, T., Shiraishi, N., "Effects of Post Combustion Chamber on Combustion Characteristics of Paraffin-Fueled Swirling Oxidizer-Flow-Type Hybrid Rocket Engine," *Space Transportation Symposium FY2012*, Institute of Space and Astronautical Science, Japan Aerospace Exploration Agency, Sagamihara, Kanagawa, Japan, 2013, STCP-2012-075. (Japanese)

[19] Sakurai, T., Yuasa, S., Anodo, H., Kitagawa, K., Shimada, T., "Performance and Regression Rate Characteristics of 5-kN Swirling-Oxidizer-Flow-Type Hybrid Rocket Engine," *Journal of Propulsion and Power*, Vol. 33, No. 4, Jul.-Aug., 2017, pp. 891-901.

doi: 10.2514/1.B36239

[20] Chelliah, H. K., Makino, A., Kato, I., Araki, N., and Law, C. K., "Modeling of Graphite Oxidation in a Stagnation-Point Flow Field Using Detailed Homogeneous and Semiglobal Heterogeneous Mechanisms with Comparisons to Experiments," *Combustion and Flame*, Vol. 104, No. 4, 1996, pp. 469–480.

doi: 10.1016/0010-2180(95)00151-4

[21] Delaney, L. J., Eagleton, L., C., and Jones W., H., "A Semiquantitative Prediction of the Erosion of Graphite Nozzle Inserts," *AIAA Journal*, Vol. 2, No. 8, 1964, pp. 1428–1433.

doi: 10.2514/3.2570

[22] Bird, R., B., Stewart, W., E., and Lightfoot, E., N., *Transport Phenomena*, 2nd ed., John Wiley & Sons, Inc., New York, 2006, Chap. 17.

[23] Bartlett, E. P., Kendall, R. M., and Rindal, R. A., "An Analysis of the Coupled Chemically Reacting Boundary Layer and Charring Ablator Part IV a Unified Approximation for Mixture Transport Properties for Multicomponent Boundary-Layer Applications," NASA-CR-1060, 1968.

[24] Svehla, R. A., "Estimated Viscosities and Thermal Conductivities of Gases at High Temperatures," NASA Lewis Research Center Technical Report, NASA-TR-R-132, 1962.

[25] McCabe W. L., and Smith, J. C., *Unit Operations of Chemical Engineering*, 3rd ed., McGraw-Hill Education, New York, 1976, Chap. 4.

[26] Kamps, L., Saito Y., Kawabata, R., Wakita, M., Totani, T., Takahashi, Y., and Nagata, H. "Method for Determining Nozzle-Throat-Erosion History in Hybrid Rockets," *Journal of Propulsion and Power*, Vol. 33, No. 6, Nov. 2017, pp. 1369-1377.

doi: 10.2514/1.B36390

[27] Matsuno, H., Kohno, M., Onoda, J., Kawashima, T., Murakami, T., and Onojima, N., "Development of the S-520 Single Stage Sounding Rocket," *Acta Astronautica*, Vol. 9, No. 10, 1982, pp. 631–635.

doi: 10.1016/0094-5765(82)90107-2

[28] Hirasawa, T., "Sounding Rocket Experiment at Syowa Station, Antarctica," *The Journal of Space Technology and Science*, Vol. 7, No. 1, 1991, pp. 1_9-1_17.

doi: 10.11230/jsts.7.1_9

[29] Yuasa, S., Kitagawa, K., Sakurazawa, T., Kumazawa, I., and Sakurai, T., "Liquid Oxygen Vaporization Techniques for Swirling-Oxidizer-Flow-Type Hybrid Rocket Engines," *International Journal of Energetic Materials and Chemical Propulsion*, Vol. 10, No. 2, 2011, 155-168.

doi: 10.1615/IntJEnergeticMaterialsChemProp.2012001351

[30] Sutton, G, P., and Biblarz O., *Rocket Propulsion Elements*, 7th ed., John Wiley & Sons, Inc., Hoboken, 2001, Chap. 3.

[31] Ben-Asher, J. Z., *Optimal Control Theory with Aerospace Applications*, AIAA, Reston, 2010, Chaps. 4 and 9.

doi: 10.2514/4.867347

[32] "Standard Atmosphere," International Organization for Standardization, ISO 2533-1975, 1975.

[33] Akiba, R., "Vertical Flight Performance of Rockets and Thrust Planning," *Bimonthly Journal of Institute of Industrial Science*, University of Tokyo, Vol. 8, No. 6, 1956, pp. 256-259 (Japanese).

[34] Goddard, R. H., "A Method of Reaching Extreme Altitudes," *Smithsonian Miscellaneous Collections*, Vol. 71, No. 2, Jan. 1920, pp. 1-79.

[35] Stark, R. H., "Flow Separation in Rocket Nozzles, a Simple Criteria," *41st AIAA/ASME/SAE/ASEE Joint Propulsion Conference & Exhibit*, AIAA, Tucson, AZ, 2005, AIAA 2005-3940.

doi: 10.2514/6.2005-3940

[36] Ozawa, K., and Shimada, T., "A Theoretical Study on Throttle Ranges of O/F Controllable Hybrid Rocket Propulsion Systems," *Journal of Fluid Science and Technology*, Vol. 13, No. 4, Nov. 2018, pp. JFST0031.

doi: 10.1299/jfst.2018jfst0031

[37] Tsiotras, P., and Kelley, H. J., "Drag-law Effects in the Goddard Problem," *Automatica*, Elsevier, Vol. 27, No. 3, May 1991, pp. 481-490.
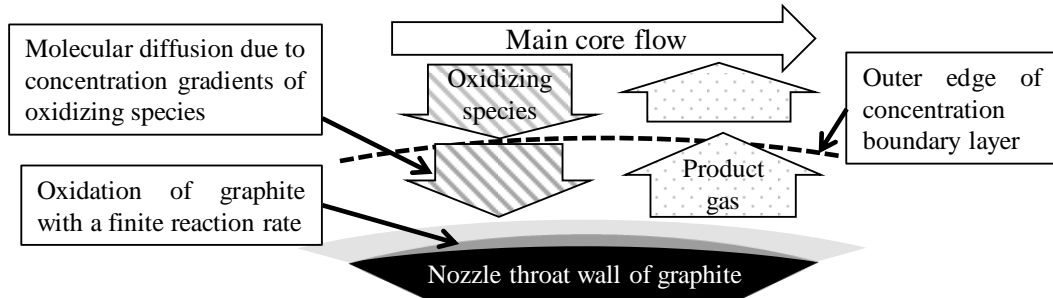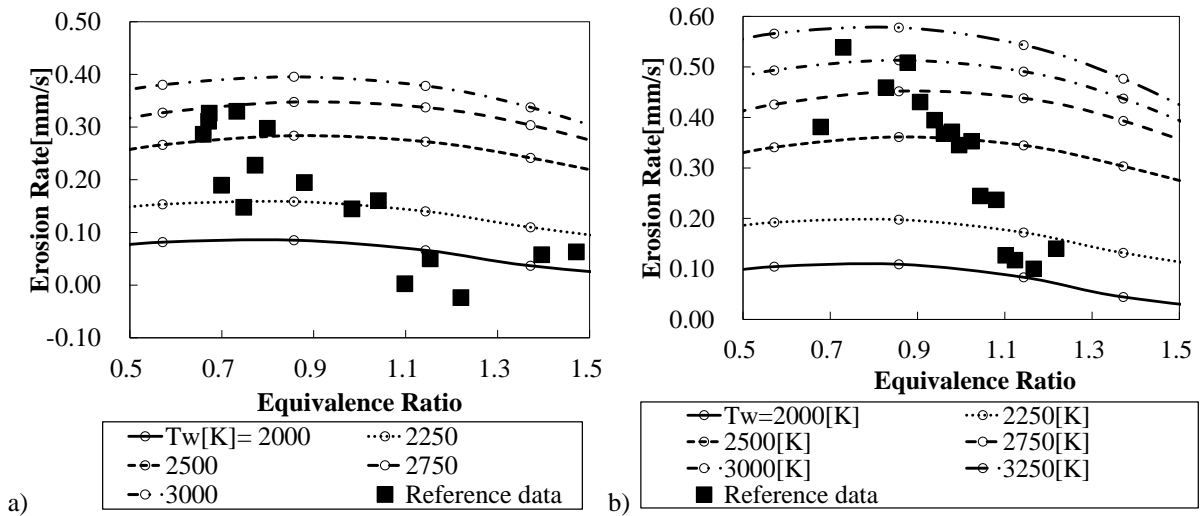
doi: 10.1016/0005-1098(91)90105-B
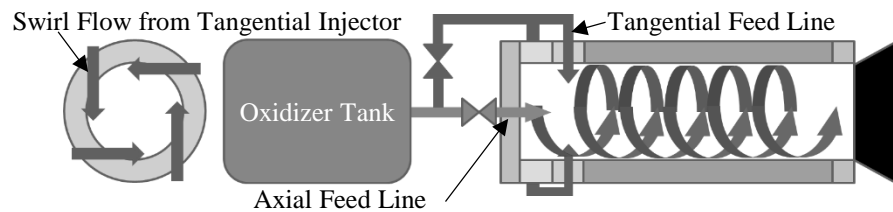
Fig. 1 Concept of Altering-intensity Swirling-Oxidizer-Flow-Type (A-SOFT) hybrid rocket engines [5].
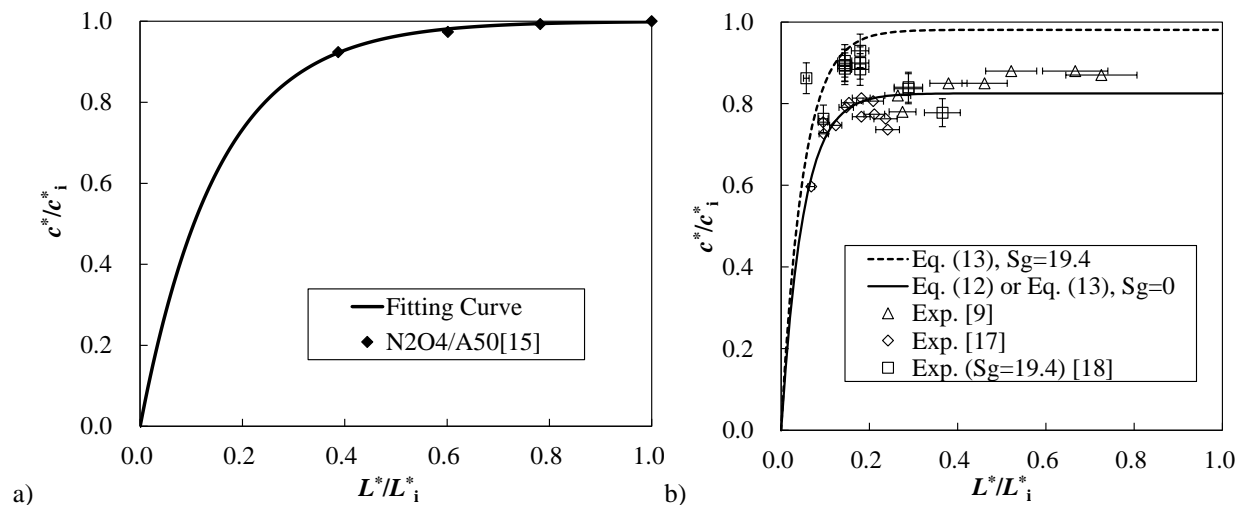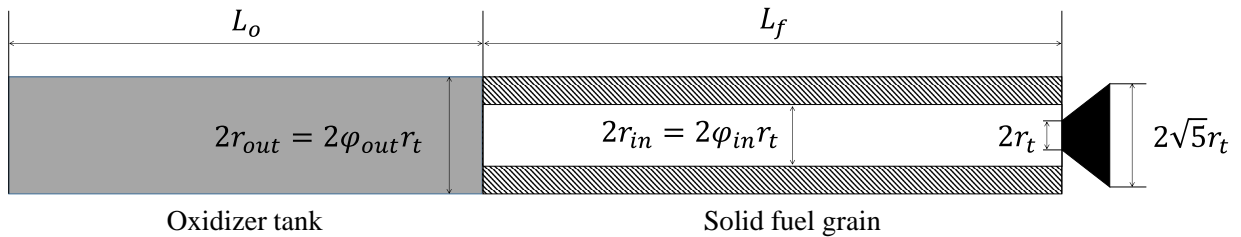
Fig. 2 Comparison of the c^* efficiency model with the experimental result a) liquid propulsion using N₂O₄ and Aerozine-50 [15] b) hybrid propulsion using paraffin wax and GOX [9][17][18].


Molecular diffusion due to concentration gradients of oxidizing species

Main core flow

Oxidizing species

Outer edge of concentration boundary layer

Oxidation of graphite with a finite reaction rate

Product gas

Nozzle throat wall of graphite

Fig. 3 Schematic of nozzle throat erosion model.

a)

b)

Fig. 4 Comparison of the throat erosion model with the experimental data [26] a) Test 1 and b) Test 4.

L_o

L_f

$2r_{out} = 2\varphi_{out}r_t$

$2r_{in} = 2\varphi_{in}r_t$

$2r_t$

$2\sqrt{5}r_t$

Oxidizer tank

Solid fuel grain

Fig. 5 Configuration of the propulsive subsystem of a hybrid sounding rocket.
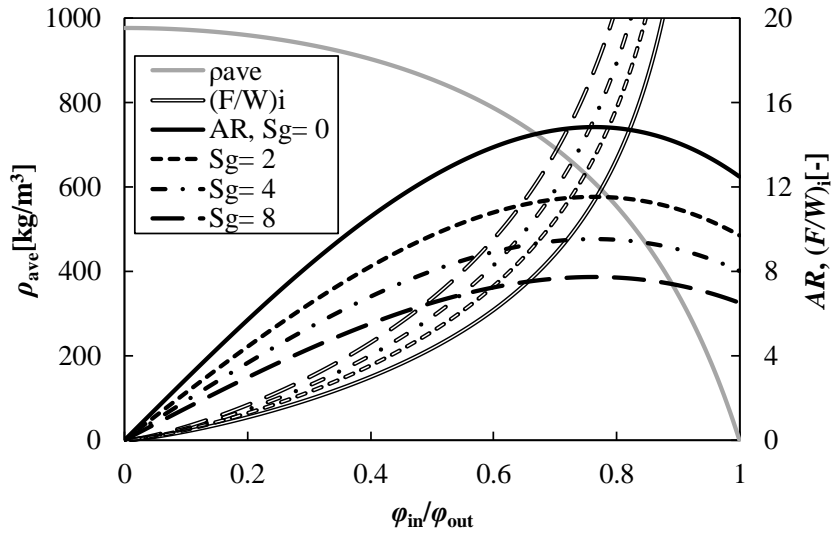
Fig. 6 Relation among S_g, $(F/W)_i$, and AR for the total mass of 2100 [kg] and the gross propellant O/F ratio

of 2.0
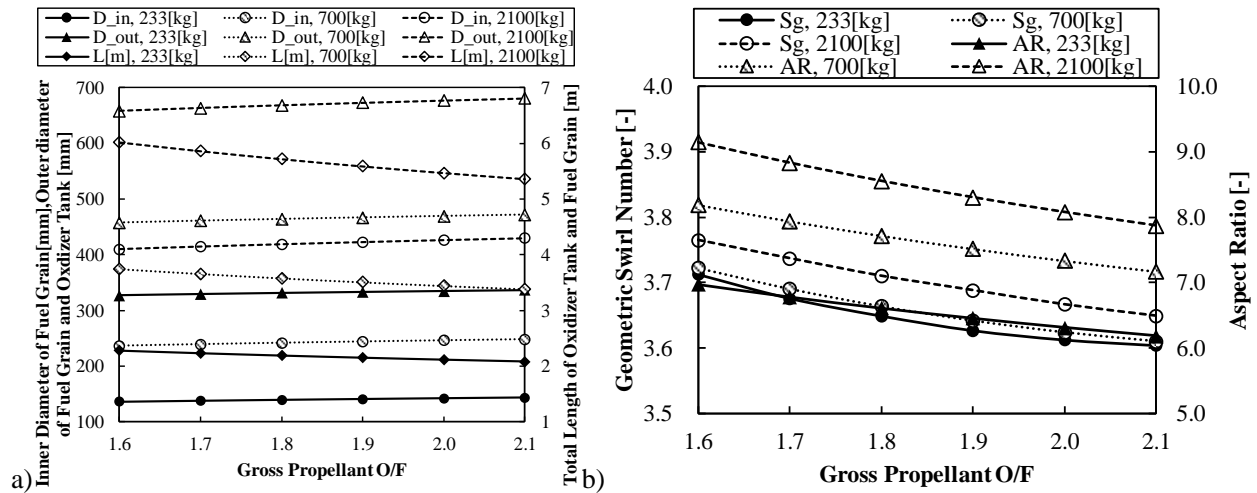
Fig. 7 Sizing of the hybrid sounding rockets: a) dimensions; b) aspect ratio and geometric swirl number of the
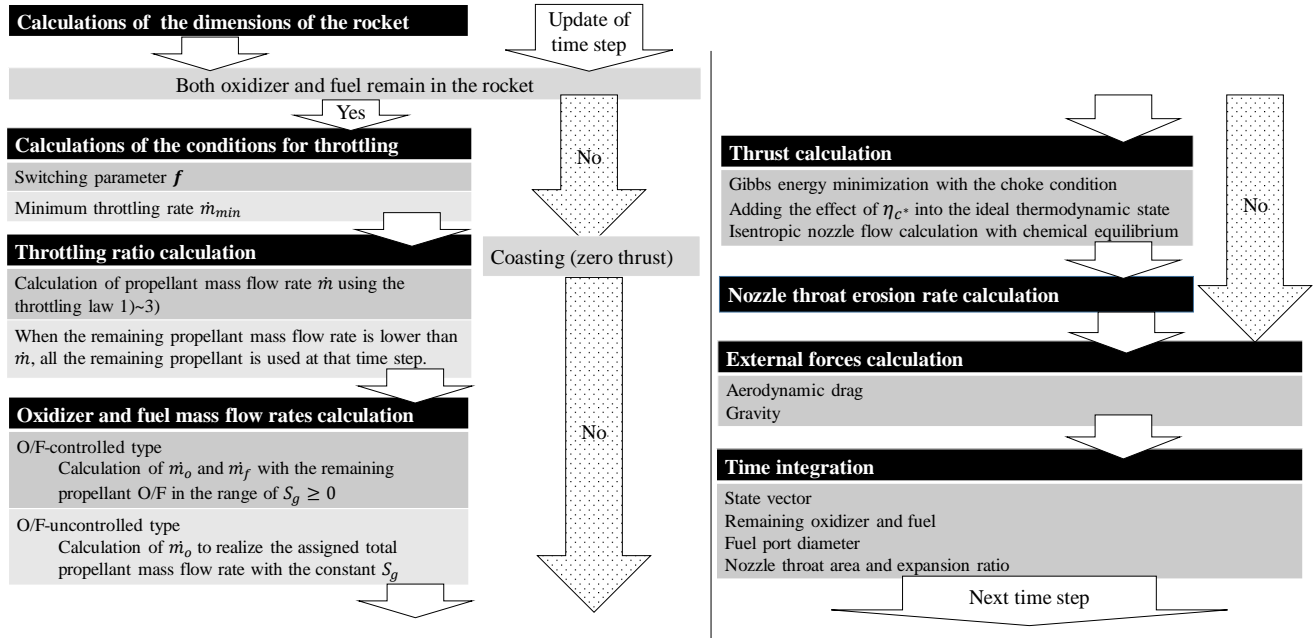
O/F-uncontrolled type.

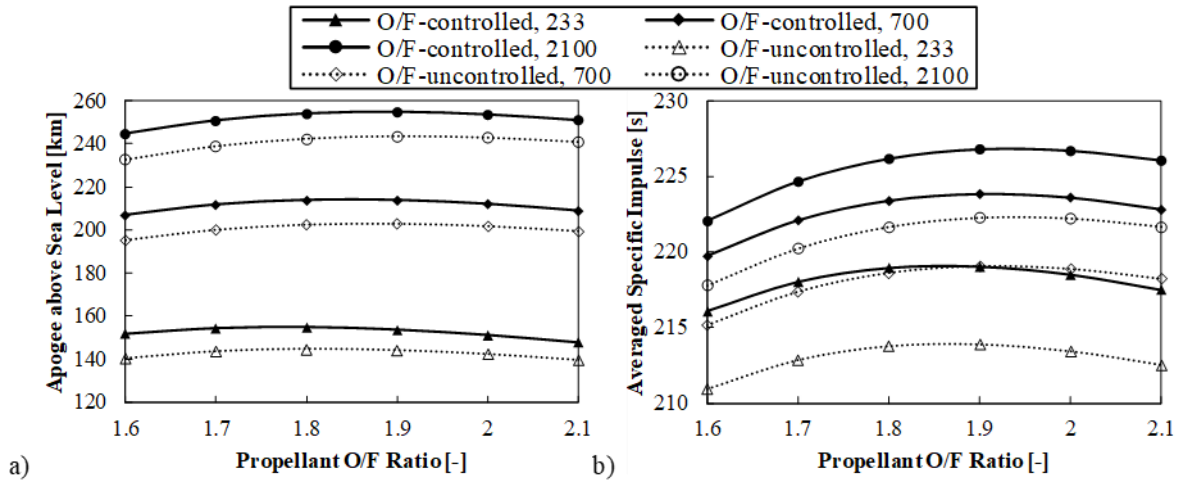**Fig. 8 Block diagram of the flight simulation program.**

Fig. 9 a) Apogee and b) weight-averaged specific impulse of the O/F-controlled and –uncontrolled hybrid sounding rockets.

Table 1 Results of the flight simulations

		O/F	1.6	1.7	1.8	1.9	2.0	2.1
O/F-	233 kg	Highest Altitude, km	151.9	154.6	155.1	153.9	151.4	147.9
		$I_{sp_{ave}}$, s	216.1	218.0	219.0	219.0	218.5	217.5
		Throat Area Increase, %	19.7	22.9	25.8	28.4	30.6	32.6
		$\eta_{c^*_{ave}}$, %	86.0	86.0	85.9	85.9	85.8	85.8

	700 kg	Highest Altitude, km	207.0	211.7	213.8	213.8	212.0	208.9
		$I_{sp_{ave}}$, s	219.7	222.1	223.4	223.8	223.6	222.8
		Throat Area Increase, %	10.2	11.9	13.4	14.8	16.0	17.1
		$\eta_{c^*_{ave}}$, %	86.0	86.0	85.9	85.9	85.9	85.9
	2100 kg	Highest Altitude, km	244.7	250.9	254.1	254.9	253.6	250.9
		$I_{sp_{ave}}$, s	222.0	224.6	226.1	226.8	226.7	226.0
		Throat Area Increase, %	5.23	6.12	6.92	7.64	8.30	8.88
		$\eta_{c^*_{ave}}$, %	86.0	86.0	85.9	85.9	85.9	85.9
O/F-uncontrolled	233 kg	Highest Altitude, km	140.5	143.7	144.8	144.2	142.4	139.7
		$I_{sp_{ave}}$, s	210.9	212.8	213.8	213.9	213.4	212.5
		Throat Area Increase, %	19.3	22.4	25.2	27.7	29.8	31.7
		$\eta_{c^*_{ave}}$, %	85.5	85.4	85.4	85.3	85.3	85.3
	700 kg	Highest Altitude, km	195.1	200.0	202.5	202.9	201.7	199.4
		$I_{sp_{ave}}$, s	215.2	217.4	218.6	219.1	218.9	218.2
		Throat Area Increase, %	10.1	11.7	13.2	14.5	15.7	16.7
		$\eta_{c^*_{ave}}$, %	85.5	85.5	85.5	85.4	85.4	85.4
	2100 kg	Highest Altitude, km	232.7	238.9	242.3	243.5	242.8	240.8
		$I_{sp_{ave}}$, s	217.8	220.2	221.6	222.2	222.2	221.7
		Throat Area Increase, %	5.21	6.06	6.84	7.54	8.16	8.70
		$\eta_{c^*_{ave}}$, %	85.5	85.5	85.5	85.5	85.5	85.4
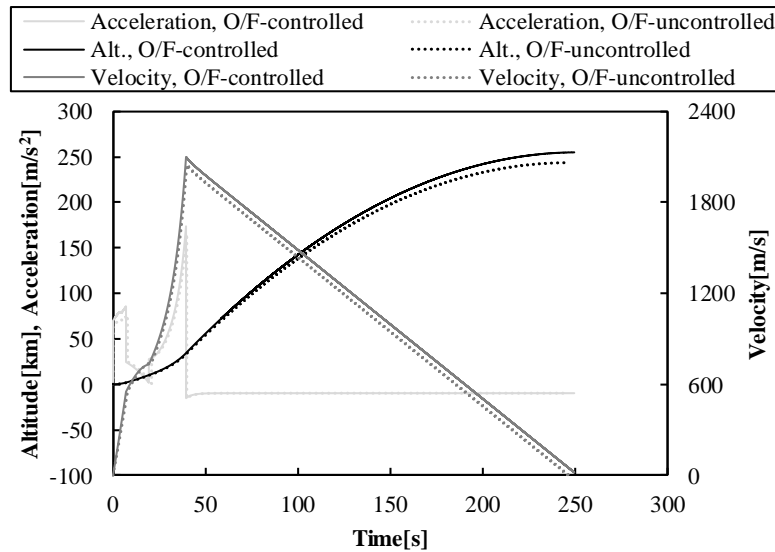
Fig. 10 Time-traces of acceleration, velocity, and altitude for the O/F-controlled and –uncontrolled hybrid sounding rockets with the gross mass of 2100 [kg].
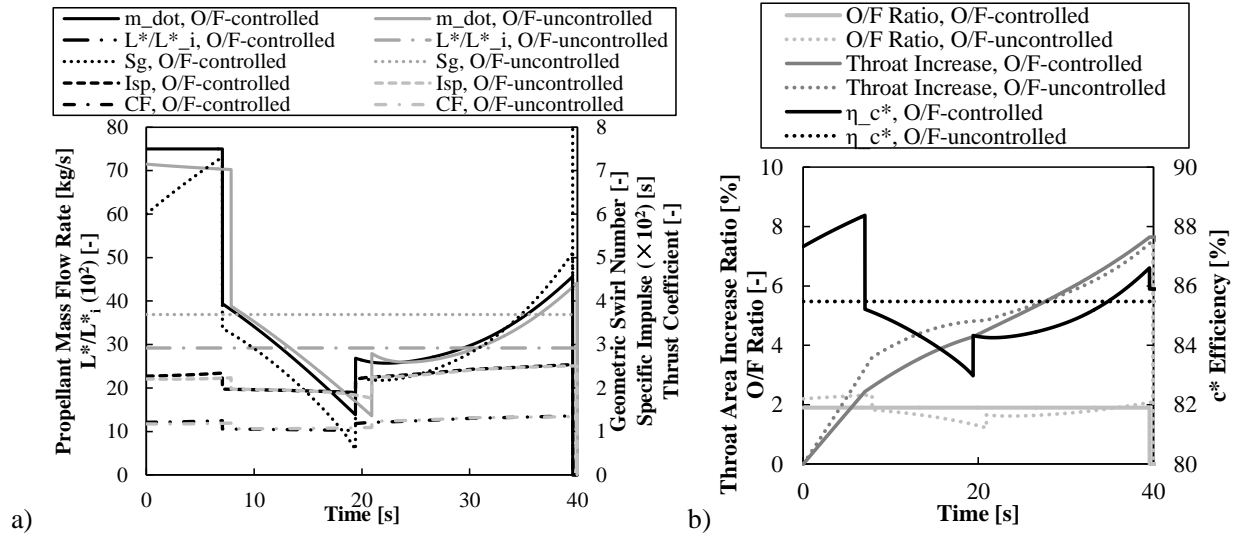
Fig. 11 Time-traces of a) propellant mass flow rate and geometric swirl number b) throat increase ratio, O/F ratio, and c^* efficiency for the O/F-controlled and –uncontrolled types with the gross mass of 2100 [kg].
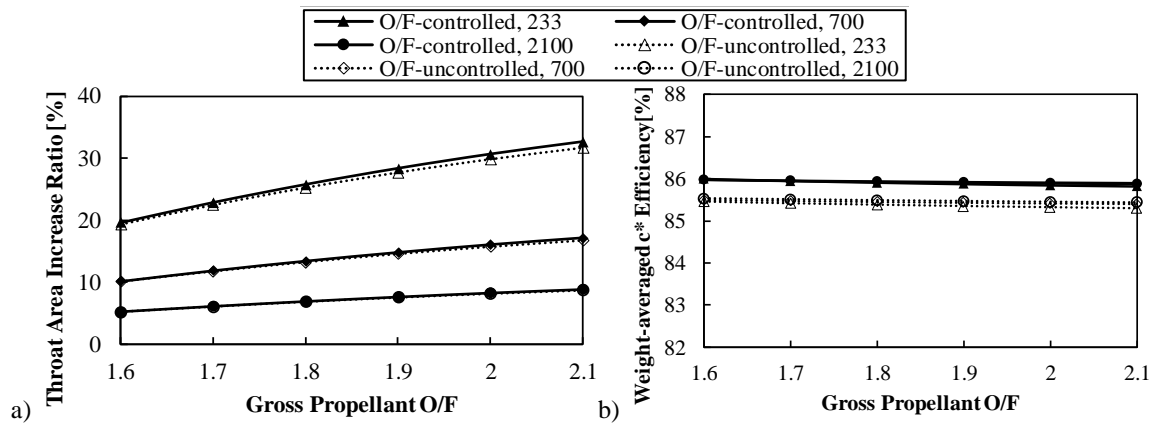

Fig. 12 a) Throat area expansion ratio and b) weight-averaged c* efficiency of the O/F-controlled and –uncontrolled types.
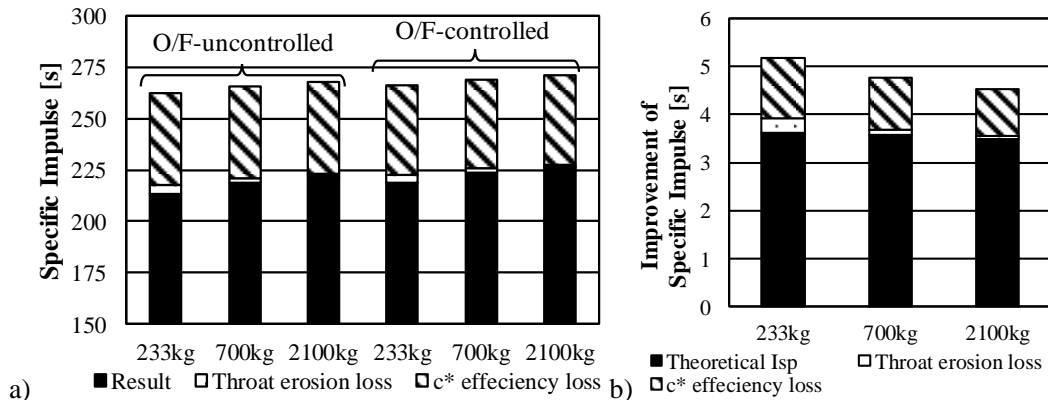
Fig. 13 a) Comparison of ideal specific impulse and specific impulse loss breakdown, b) share estimations of the specific impulse improvement.
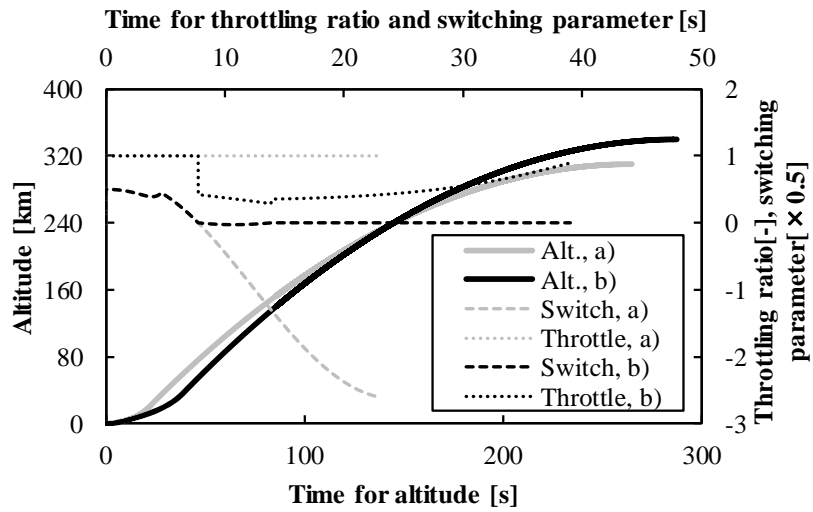

Fig. 14 Comparison of performance between the thrust control laws a) and b).